



# Spatio-temporal dynamics of an SIS model with nonlinear incidence and nonlocal disease transmission

Dhiraj Kumar Das · S. Ghorai · Malay Banerjee

Received: 6 March 2023 / Accepted: 28 May 2023 / Published online: 19 June 2023  
© The Author(s), under exclusive licence to Springer Nature B.V. 2023

**Abstract** Investigation of the spatio-temporal patterns exhibited by infected communities sharing the same spatial region is the focus of many researchers. Typically, an individual's susceptibility is substantially connected with the distance from nearby affected persons. Such a disease propagation mechanism is called the nonlocal infection which is primarily modeled with a kernel function  $K$ , whose support determines the range of the nonlocal infection area. In our current study, a susceptible–infected–susceptible-type epidemic model is analyzed considering the nonlinear disease incidence rate which is further extended to incorporate the nonlocal disease transmission and random movement of the individuals. Complete bifurcation characteristics of the associated temporal model include the saddle-node, subcritical Hopf, and homoclinic bifurcations. Our primary emphasis is to investigate the formation of a wide variety of spatio-temporal patterns that include stationary, quasi-periodic, periodic, and chaotic patterns, among others. Comparisons have been made between the spatio-temporal dynamics of the local and nonlocal disease transmission models. It is observed that the nonlocal disease transmission

expands the parametric domain (referred to as Hopf and stable domains) on which the system possesses oscillatory and spatially homogeneous solutions. As a result, the spatially heterogeneous stationary solutions (referred to as Turing patterns) of the local system turn into irregular oscillatory solutions or spatially homogeneous solutions whenever the nonlocal extent of the disease transmission gradually increases. Also, the increased range of nonlocal infections reduces the number of stationary patches. In addition, the system exhibits “long transient” dynamics when the dispersal rate of the population tends to the Turing threshold. Exhaustive numerical simulations have been carried out to illustrate the wide range of spatio-temporal patterns displayed by the system in the presence and absence of nonlocal terms.

**Keywords** SIS epidemic model · Nonlocal infection · Spatio-temporal dynamics · Turing instability · Transient dynamics

## 1 Introduction

Analysis of the spread of communicable diseases is crucial to understand the underlying transmission mechanism of the disease. The elementary mathematical setup for this type of investigation is almost a century old and was framed by Kermack and McKendrick in 1927 [1]. They compartmentalized the total community into three disjoint sets according to individ-

D. K. Das (✉) · S. Ghorai · M. Banerjee  
Department of Mathematics and Statistics, Indian Institute of Technology Kanpur, Kanpur, Uttar Pradesh 208016, India  
e-mail: dhirajkd@iitk.ac.in

S. Ghorai  
e-mail: sghorai@iitk.ac.in

M. Banerjee  
e-mail: malayb@iitk.ac.in

ual clinical status namely susceptible, infected, and recovered. The interactions among the compartments followed by switching individual's clinical stage were described by coupled differential equations known as the SIR-epidemic model. After this paradigmatic work, several epidemic models were proposed and analyzed by numerous researchers [2–4]. The outcomes of these models are often useful in disease prevention, control, prediction, and other public health welfare.

The compartmental epidemic models come in a variety of forms depending upon the characteristics of the transmissible diseases. In particular, the number of compartments in an epidemic model is equal to the distinct clinically identifiable stages of the disease. For example, the SIR-type epidemic models are suitable to describe the disease in which individuals acquire immunity after a successful recovery. The SEIR-type epidemic models assume an exposed compartment  $E$  to represent the incubation stage where an individual is infected but not yet infectious. In addition, more complicated compartmental structures are possible which include vaccination, quarantine, hospitalization, different level of infectious stages, etc. A systematic formulation of the different types of epidemic models can be found in [5–7]. In this study, we consider an SIS-type epidemic model assuming that the transmissible disease does not confer immunity after recovery. This assumption confines the system to two compartments which can be used to study the transmission dynamics of many infectious diseases in humans and animals. Moreover, the simplest nature of the SIS-type models is favorable for mathematical analysis in reaction–diffusion setup.

In modeling the transmission of infectious diseases, the adopted per-capita disease incidence rate plays a central role in determining the dynamic behavior of the entire system. Most of the existing literature is based on bilinear-type incidence rate  $\beta SI$ , where  $S$  and  $I$  denote the densities of the susceptible and infectious present in a population with constant disease transmission rate  $\beta > 0$ . It relies on the linear interaction assumption between the  $S$  and  $I$  populations. However, this assumption may not be realistic or may be inefficient in mirroring disease transmission mechanisms when the population undergoes saturation effect or behavioral responses to avoid the risk of infections. Hence, some researchers proposed epidemic models taking into account the nonlinear disease incidence rates of various forms to address diverse complexities involved

in disease transmission [8,9]. A general form of these kinds of incidence rates may be described by  $\beta g(I)S$ , where  $g(.)$  is a continuous real-valued function. A wide range of qualitative differences in the dynamical characteristics is reported in the studies of epidemic models with nonlinear incidence rates compared to their bilinear counterparts. Epidemic models with bilinear-type incidence rates exhibit classical patterns in which the disease eradication is confirmed by monitoring a threshold value called basic reproduction number [10]. However, periodic solutions appear through Hopf bifurcation in models with nonlinear incidence rates and persistence of multiple endemic equilibria turns the system into multistable in nature [11]. Therefore, the presence of nonlinearity in disease incidence rates results in complexity in the qualitative dynamics of the system which causes more challenges and less predictability in preventing disease transmission.

The influence of the spatial mobility of two interacting communities on the spatial distribution of the population is widely investigated using reaction–diffusion equations [12,13]. The diffusion-driven instability, which is also known as Turing instability, is often used to explain various patterns exhibited by interacting populations in their natural habitat [14–17]. Further, the interplay between the susceptible and infected individuals in a community or species suffering from a contagious disease is conditionally similar to prey–predator interaction [18]. Therefore, to investigate the spatial heterogeneity many theoretical epidemiologists extended the temporal epidemic models into reaction–diffusion system by simply introducing a diffusion term [19–21]. Reaction–diffusion systems representing epidemic models exhibit spatio-temporal patterns [22,23] and traveling wave solutions [24–27]. A spatio-temporal pattern represents the distribution of the population both along space and time, whereas a traveling wave represents the transition of infection from one location to another. Our primary objective in this study is to explore the spatio-temporal patterns. A systematic review of the patterns exhibited by epidemic models can be found in [22].

In spite of the functional similarity in addressing the disease incidence rate and predation, there are many fundamental differences between these two mechanisms. Thus, special treatment is required to study the interaction both in mathematical epidemiology and eco-epidemiology [18]. However, very few attempts have been made to address this important issue. An

essential difference between these two mechanisms is the spatial location of the interacting individuals from different compartments. In particular, both the prey and predator must be present at the same spatial location for predation. On the other hand, an infectious individual can infect a distant susceptible individual when the causative agent of the disease can flow by air, water, or through any other communicable media. Therefore, it is reasonable to assume that the transmission of diseases is a nonlocal mechanism. Interaction or coupling between individuals present at different spatial locations allows the infection to spread to a wider range and acts to synchronize the epidemic dynamics. This type of behavior can be captured in an epidemic model by introducing a transmission kernel,  $K$ , which modifies the disease incidence rate and is a function of the distance between two individuals [5, 27, 28]. In particular, the modified incidence rate for a bounded interval  $\Omega$  in one-dimensional space is given by

$$\lambda(x, t; I) = \beta \int_{\Omega} I(y, t) K(x - y) dy,$$

which models the total transmission force exerted at the spatial location  $x$  at time  $t$  from other points  $y$  located in  $\Omega$ . Here,  $\beta$  denotes the transmission rate of the disease. The transmission risk is expected to reduce as the spatial distance  $|x - y|$  between the susceptible and infected individuals increases which must be an inherent feature of the transmission kernel  $K$ . Typically,  $K$  is a compactly supported probability density function on  $\mathbb{R}$  and  $K(x - y)$  weighs the contribution of an infected at a spatial location  $y$  toward infecting a susceptible individual at the location  $x$ . This modifies the system of ordinary differential equations to a system of integro-differential equations (IDEs).

In our current study, within a reaction–diffusion setting, we consider an SIS (susceptible–infected–susceptible) model with a nonlinear incidence rate as in [29, 30]. The nonlocal incidence may be attributed to several epidemiological aspects like the behavioral response, saturation effect, heterogeneous mixing of population, crowding effect, etc. Though the empirical data of infectious diseases are insubstantial in several aspects, given a situation, the exact justification of nonlocal incidence rate lies upon the critical understanding of disease transmission mechanism. For example, in an abundance of infected individuals, exposure to the causative agents is more likely and hence less than a linear response could occur due to saturation. In contrast, given a very low density of infected or diseases

that requires multiple exposures to transmit, more than a linear response is suitable in modeling prospects. Further, we extend the local model to a nonlocal framework by considering a suitable transmission kernel function. In recent times, a considerable number of studies have been carried out to understand the influence of nonlocal interactions among species of spatio-temporal models. For example, spatio-temporal pattern formation, in the presence of nonlocal interaction in the prey population, has been studied by Pal et al. [31, 32]. Their investigation has shown extensive qualitative changes in pattern formation in the presence of nonlocal interaction characterized by various spatial kernels. Further, a generalized version of a three-species cyclic competition model in presence of nonlocal intra-specific competition has been investigated for spatial pattern formation by Manna et al. [33]. Also, a nonlocal interaction between prey and predator has been introduced by Banerjee et al. [34]. Some more recent results concerning the spatio-temporal dynamics due to nonlocal interaction in biological and biomedical models can be found in [35–37]. Nevertheless, the existing literature on the formation of spatio-temporal patterns considers only the local infection between the susceptible and infected populations [38, 39]. These models exhibit a variety of both stationary and dynamic patterns. Therefore, a natural question arises regarding the consequences of the nonlocal infection on the formation of spatio-temporal patterns, which is yet to be attempted. It is expected that the presence of nonlocal terms will significantly alter the spatio-temporal dynamics. Our primary objective in this study is to identify these qualitative changes through spatio-temporal asymptotic analysis and discuss the corresponding epidemiological significance. To the best of our knowledge, there does not exist any investigation on the effect of nonlocal disease transmission on spatio-temporal pattern formation. Apart from the asymptotic analysis, we have also discussed the transient dynamics produced by the proposed SIS model. It has been observed that many biological systems undergo a “long transient” before reaching the final state [40–42]. The study of phase transition is essential to understand the sudden change in the dynamics and the presence of ghost attractors. Consequently, it helps in assessing epidemics across human, wildlife, and agricultural systems and designing effective management strategies to combat them [43].

This paper is organized as follows. The temporal SIS model with nonlinear disease incidence term is introduced in Sect. 2 which also discusses the existence of equilibrium points. A complete bifurcation analysis of the temporal model along with graphical visualization for a given dataset is presented in Sect. 3. The temporal model is extended spatially in Sect. 4, where Turing instability of a homogeneous endemic steady state is also discussed. The spatial model is further extended to incorporate the nonlocal disease transmission using a distance transmission kernel in Sect. 5. Here, we have again examined the Turing instability condition of the same endemic steady state. The spatio-temporal patterns exhibited by both the local and nonlocal models are explored with the help of numerical simulations in Sect. 6. The same section also contains the “long transient” behavior exhibited by the system. Finally, we summarize our findings and discuss their epidemiological significance in Sect. 7.

## 2 Mathematical model

The paradigmatic work of Kermack and McKendrick [1] considers a compartmental epidemic model, known as SIR model, which is a system of coupled ordinary differential equations. Thereafter, many theoretical epidemiologists carried out their investigations in order to study several critical mechanisms of infectious disease transmission and its control. Typical per-capita disease incidence rates, used in most of the epidemic models, are linear in nature. However, it may not be suitable for all the cases and often misses the vital transmission dynamics described by the contagion due to saturation, multiple exposures, inhibition effect followed by the behavioral changes in susceptible, heterogeneous mixing of population, etc. [44, 45]. Liu et al. [29, 30] described an epidemic model with a nonlinear incidence rate of the form  $\beta I^p S^q$ , where  $\beta, p, q > 0$ , and their investigations revealed a wide range of qualitative differences compared to those of epidemic models with standard linear incidence rate. The qualitative dynamics change significantly when  $p$  is different from unity. However, the nonlinearity in  $S$  does not alter the dynamics qualitatively and it is not epidemiologically justifiable.

Let  $S(t)$  and  $I(t)$  be the densities of the susceptible and infectious populations, respectively. The model equations are

$$\begin{aligned}\frac{dS}{dt} &= \Lambda - \beta SI^2 + \gamma I - \mu S, \\ \frac{dI}{dt} &= \beta SI^2 - (\gamma + \sigma + \mu)I,\end{aligned}\quad (1)$$

with non-negative initial conditions  $S(0) = S_0$  and  $I(0) = I_0$ . The parameters of the model are disease transmission rate  $\beta$ , constant recruitment rate to the susceptible population  $\Lambda$ , natural mortality rate of the whole population  $\mu$ , recovery rate of the infected individual  $\gamma$ , and the disease-induced mortality rate of infected individual  $\sigma$ . Also, it is assumed that recovery does not give any immunity to the disease and hence recovered becomes susceptible to the disease instantaneously.

### 2.1 Equilibrium points and their stability

System (1) always possesses a disease-free equilibrium point  $P_0 = (\frac{\Lambda}{\mu}, 0)$ . A co-existing equilibrium point or the endemic equilibrium  $P^* = (S^*, I^*)$  satisfies

$$\begin{aligned}\beta S^* I^* - (\gamma + \sigma + \mu) &= 0, \\ \Lambda - \beta S^*(I^*)^2 + \gamma I^* - \mu S^* &= 0.\end{aligned}\quad (2)$$

Eliminating  $S^*$  from these two equations, we find

$$a_2(I^*)^2 + a_1 I^* + a_0 = 0, \quad (3)$$

where  $a_2 = \beta(\sigma + \mu)$ ,  $a_1 = -\Lambda\beta$  and  $a_0 = \mu(\gamma + \sigma + \mu)$ .

For a feasible endemic equilibrium point, we must have a positive root of the quadratic equation (3). Using Descartes' rule of signs, we conclude that the system has either two or zero positive roots. The discriminant of the quadratic equation (3) is given by

$$D = a_1^2 - 4a_0a_2 = \beta\Lambda^2(\beta - \beta_c),$$

where  $\beta_c = \frac{4\mu(\gamma + \sigma + \mu)(\sigma + \mu)}{\Lambda^2}$ .

It is clear that Eq. (3) has two distinct real roots when  $\beta > \beta_c$ . These two real roots coincide at  $\beta = \beta_c$  leading to a unique endemic equilibrium point. Finally, the roots of Eq. (3) are

$$I_{1,2}^* = \frac{\Lambda}{2(\sigma + \mu)} \left( 1 \pm \sqrt{1 - \frac{\beta_c}{\beta}} \right).$$

Thus, the endemic equilibria are given by  $P_{1,2}^* = (S^*, I^*) = (\frac{\gamma+\sigma+\mu}{\beta I_{1,2}^*}, I_{1,2}^*)$ . We keep the parameters  $\Lambda$ ,  $\mu$ ,  $\gamma$ ,  $\sigma$  fixed and choose  $\beta$  as a bifurcation parameter. The Jacobian matrix of system (1) at the endemic equilibrium point  $(S^*, I^*)$  is given by

$$\mathcal{J} = \begin{bmatrix} -\beta(I^*)^2 - \mu & -2\beta I^* S^* + \gamma \\ \beta(I^*)^2 & 2\beta I^* S^* - (\gamma + \sigma + \mu) \end{bmatrix}$$

$$\equiv \begin{bmatrix} a_{11} & a_{12} \\ a_{21} & a_{22} \end{bmatrix}. \quad (4)$$

The trace and determinant of the Jacobian matrix are

$$\text{Trace}(\mathcal{J}) = a_{11} + a_{22} = (\sigma + \gamma) - \beta(I^*)^2,$$

and

$$\begin{aligned} \text{Det}(\mathcal{J}) &= a_{11}a_{22} - a_{12}a_{21} \\ &= (\sigma + \mu)\beta(I^*)^2 - (\gamma + \sigma + \mu)\mu. \end{aligned} \quad (5)$$

We need  $\text{Trace}(\mathcal{J}) < 0$  and  $\text{Det}(\mathcal{J}) > 0$  for local asymptotic stability of the endemic equilibrium point. Further, the equilibrium is a saddle point if  $\text{Det}(\mathcal{J}) < 0$ .

**Proposition 1** *The disease-free equilibrium  $P_0$  is always locally asymptotically stable.*

*Proof* The Jacobian matrix  $\mathcal{J}$  has two negative eigenvalues  $-\mu$  and  $-(\gamma + \sigma + \mu)$  whenever  $I^* = 0$ . Therefore,  $P_0$  is always locally asymptotically stable.  $\square$

**Proposition 2** *The endemic equilibrium point  $P_2^* = (S^*, I_2^*)$  is always a saddle point.*

*Proof* Substituting the expression of  $(I^*)^2$  from (3) into (5) and then simplifying, we find

$$\begin{aligned} \text{Det}(\mathcal{J})|_{P_2^*} &= \frac{\Lambda^2 \beta}{2(\sigma + \mu)} \left[ \left(1 - \frac{\beta_c}{\beta}\right) \right. \\ &\quad \left. - \sqrt{1 - \frac{\beta_c}{\beta}} \right], \quad \forall \beta \geq \beta_c. \end{aligned} \quad (6)$$

Since  $0 \leq \left(1 - \frac{\beta_c}{\beta}\right) < 1$ ,  $\forall \beta \geq \beta_c$ , we conclude that  $\text{Det}(\mathcal{J})|_{P_2^*} \leq 0$  whenever  $\beta \geq \beta_c$  and the equality occurs only at  $\beta = \beta_c$ . Therefore,  $P_2^*$  is always a saddle point for  $\beta > \beta_c$ .  $\square$

**Proposition 3** *The local asymptotic stability of  $P_1^*$  depends on the sign of  $\text{Trace}(\mathcal{J})|_{P_1^*}$ .*

*Proof* The determinant of the Jacobian matrix described in (4) at the endemic equilibrium point  $P_1^* = (S^*, I_1^*)$  is

$$\begin{aligned} \text{Det}(\mathcal{J})|_{P_1^*} &= \frac{\Lambda^2 \beta}{2(\sigma + \mu)} \left[ \left(1 - \frac{\beta_c}{\beta}\right) \right. \\ &\quad \left. + \sqrt{1 - \frac{\beta_c}{\beta}} \right], \quad \forall \beta \geq \beta_c, \end{aligned} \quad (7)$$

which is positive whenever  $\beta > \beta_c$ . Therefore, the stability of  $P_1^*$  depends on the sign of  $\text{Trace}(\mathcal{J})|_{P_1^*}$ .  $\square$

### 3 Local bifurcation analysis

Model (1) is capable of exhibiting two local bifurcations, namely a saddle-node bifurcation related to the generation of an endemic equilibrium and a Hopf bifurcation related to the destabilization of stable endemicity.

#### 3.1 Saddle-node bifurcation

**Proposition 4** *System (1) undergoes a saddle-node bifurcation with respect to the parameter  $\beta$  at the critical point  $\beta_c$ .*

*Proof* Note that two endemic equilibria collide when  $\beta = \beta_c$  leading to a single endemic equilibrium point

$$P_{SN}^* = \left( \frac{\gamma + \sigma + \mu}{\beta_c I_{SN}^*}, I_{SN}^* \right), \quad \text{where } I_{SN}^* = \frac{\Lambda}{2(\sigma + \mu)}.$$

Further, we observe that  $\text{Det}(\mathcal{J}; \beta_c, I_{SN}^*) = 0$ . Hence, the Jacobian matrix (4) has a simple zero eigenvalue at  $P_{SN}^*$ . Let  $v = (1, \phi)^T$  and  $w = (\psi, 1)^T$  be the left and right eigenvectors corresponding to the zero eigenvalue of the Jacobian matrix at  $P_{SN}^*$ . We write that right-hand side of system (1) as  $F = (f, g)^T$  and verify that

$$\begin{aligned} w^T F_\beta(P_{SN}^*; \beta_c) &= \frac{\Lambda^2(2\gamma + 3(\sigma + \mu))}{4\mu(\sigma + \mu)(\gamma + 2(\sigma + \mu))} \neq 0, \\ w^T D^2 F(P_{SN}^*; \beta_c)v &= \gamma + \sigma + \mu \neq 0. \end{aligned}$$

Thus, the transversality conditions of the saddle-node bifurcation are satisfied, and system (1) undergoes a saddle-node bifurcation with respect to the parameter  $\beta$  at  $\beta = \beta_c$ .  $\square$

*Remark 1* Unlike other epidemic models, here the endemic equilibrium is generated through a saddle-node bifurcation instead of a transcritical bifurcation.

#### 3.2 Hopf bifurcation

From Proposition 3, it is clear that the endemic equilibrium  $P_1^*$  is locally asymptotically stable when  $\text{Trace}(\mathcal{J})|_{P_1^*} < 0$ . Hence,  $P_1^*$  becomes unstable whenever  $\text{Trace}(\mathcal{J})|_{P_1^*} > 0$ . Hopf-bifurcation threshold is

given by  $\text{Trace}(\mathcal{J}) = 0$ , which on simplification yields a critical value  $\beta_h$  of the parameter  $\beta$  given by

$$\beta_h = \frac{\{(\gamma + \sigma)(\sigma + 2\mu) + \mu^2\}^2}{\Lambda^2(\sigma + \gamma)}. \quad (8)$$

Further, it is observed that

$$\begin{aligned} \text{Det}(\mathcal{J})|_{P_1^*} &> 0 \text{ and } \frac{d}{d\beta} \\ \left[ \text{Trace}(\mathcal{J})|_{P_1^*} \right] &\neq 0 \text{ at } \beta = \beta_h. \end{aligned} \quad (9)$$

Hence, we arrive at the following proposition:

**Proposition 5** *The endemic equilibrium  $P_1^*$  undergoes a Hopf bifurcation at  $\beta = \beta_h$ .*

A limit cycle surrounding the endemic equilibrium  $P_1^* = (S_1^*, I_1^*)$  appears near the Hopf-bifurcation threshold  $\beta = \beta_h$ , and the stability of the bifurcating limit cycle can be determined from the first Lyapunov coefficient  $\mathcal{L}_1$ . The Hopf bifurcation is supercritical when  $\mathcal{L}_1$  is negative at  $\beta = \beta_h$  and hence generates a stable limit cycle around the equilibrium point. However, if  $\mathcal{L}_1$  is positive at  $\beta = \beta_h$ , then it generates an unstable limit cycle and the system undergoes subcritical Hopf bifurcation. We shall verify the sign of  $\mathcal{L}_1$  with the help of a numerical example.

### 3.3 Numerical results for the temporal model

Now, we present some numerical simulations of the temporal system (1) to visualize the analytical findings discussed above. We fix the parameter values  $\Lambda = 1$ ,  $\mu = 1$ ,  $\sigma = 1.8$ ,  $\gamma = 1$  and vary the bifurcation parameter  $\beta$ . Figure 1 illustrates the three different cases of the existence of endemic equilibria. The endemic states appear at the threshold value  $\beta = \beta_c \approx 42.56$  via a saddle-node bifurcation and exist for  $\beta > \beta_c$ . Figure 1 clearly demonstrates that system (1) possesses no endemic equilibrium point for  $\beta < \beta_c$ . Therefore, an increase in the disease transmission rate  $\beta$  leads to the appearance of the endemic states through a saddle-node bifurcation.

The local and global bifurcations exhibited by system (1) are displayed in Fig. 2. The two branches of equilibria that appear at the saddle-node bifurcation threshold  $\beta = \beta_c$  are unstable, and these are shown by the dashed magenta-colored curves. Further, between these two unstable branches of endemic steady states, the one with lesser infected ( $P_2^*$ ) remains saddle throughout. The other endemic state ( $P_1^*$ ) emerges

as an unstable spiral node and remains the same for  $\beta \in (\beta_c, \beta_h) \approx (42.56, 48.39)$ . The first Lyapunov coefficient  $\mathcal{L}_1$  of the system is positive at  $\beta = \beta_h$ , and hence, the emerged limit cycle due to the Hopf bifurcation is unstable in nature, shown as dashed blue-colored curves in Fig. 2. Thus, system (1) exhibits a subcritical Hopf bifurcation at  $\beta = \beta_h$ . Further increment in  $\beta$  increases the amplitude of the unstable limit cycle which finally disappears through a homoclinic bifurcation at  $\beta \approx 49.50$ . The associated phase portraits of system (1) near the Hopf-bifurcation threshold  $\beta = \beta_h$  are illustrated in Fig. 3. Figure 3a shows the phase diagram for  $\beta = 49.2 > \beta_h$ . The stable and unstable manifolds of the saddle point  $P_2^*$  (denoted by a blue dot) are plotted in magenta- and red-colored curves, respectively. The green dot denotes the stable endemic point  $P_1^*$  around which the unstable limit cycle is plotted in magenta color. This unstable limit cycle emerges due to subcritical Hopf bifurcation at  $\beta = \beta_h$ . If we increase  $\beta$  to 49.50, the unstable manifold returns back to the saddle point  $P_2^*$  through a homoclinic loop shown in Fig. 3b. Therefore, system (1) undergoes a homoclinic bifurcation at  $\beta = 49.50$ . Further, the unstable limit cycle disappears for  $\beta = 50 > 49.50$  and the unstable manifold of  $P_2^*$  converges to both  $P_1^*$  and the disease-free equilibrium  $P_0$  as shown in Fig. 3c. It is observed that the basin of attraction of  $P_1^*$  is confined inside the unstable limit cycle till the global homoclinic bifurcation at  $\beta = 49.50$ . But, the stable manifold of  $P_2^*$  creates the separatrix between the basin of attractions of the attractors  $P_0$  and  $P_1^*$  for  $\beta > 49.50$  (see Fig. 3c).

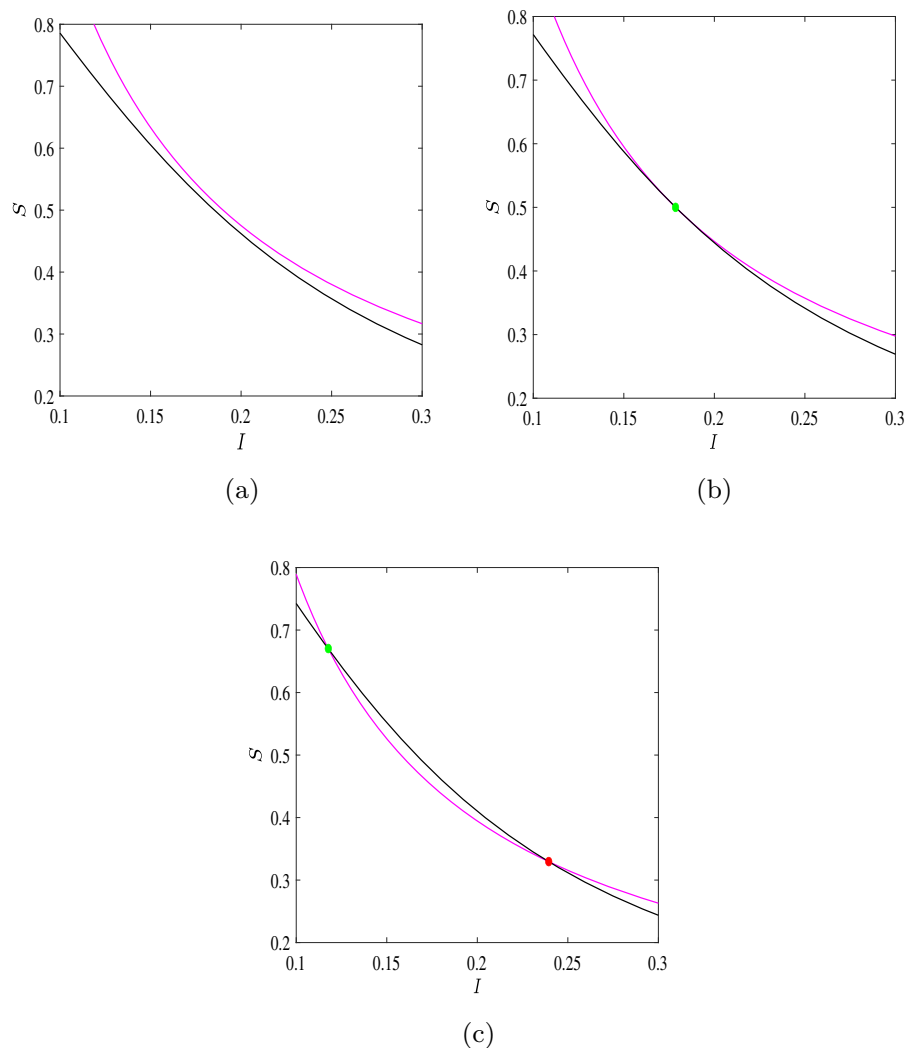
## 4 The spatio-temporal model

The random movement of the population species can be incorporated by introducing diffusion to the model system (1). A one-dimensional spatial domain  $(-L, L)$  is considered with the boundary  $\partial\Omega = \{L, -L\}$ . The governing equations are

$$\begin{aligned} \frac{\partial S}{\partial t} &= \Lambda - \beta SI^2 + \gamma I - \mu S + d_1 \frac{\partial^2 S}{\partial x^2}, \\ \frac{\partial I}{\partial t} &= \beta SI^2 - (\gamma + \sigma + \mu)I + d_2 \frac{\partial^2 I}{\partial x^2}, \quad x \in (-L, L), t > 0, \end{aligned} \quad (10)$$

where  $d_1$  and  $d_2$  represent the diffusion coefficients of susceptible and infected species, respectively. The system is subjected to non-negative initial and periodic boundary conditions.

**Fig. 1** Plot of nontrivial nullclines of system (1) for different values of  $\beta$ : **a**  $\beta = 40 < \beta_c$ , **b**  $\beta = \beta_c \approx 42.56$ , and **c**  $\beta = 48.155 > \beta_c$ . The magenta- and black-colored curves represent the nontrivial infected and susceptible nullclines, respectively. Panels **a**, **b**, and **c** show the non-existence of an endemic equilibrium point, a unique equilibrium point (green dot), and two distinct endemic equilibria (green and red dots), respectively. Other parameter values are  $\Lambda = 1$ ,  $\mu = 1$ ,  $\sigma = 1.8$  and  $\gamma = 1$ .



#### 4.1 Turing instability

Spatially co-existing homogeneous steady-state solutions of system (10) correspond to the endemic equilibria  $P_1^*$  and  $P_2^*$  of the temporal model (1). We have observed that the endemic equilibrium  $P_1^*$  is asymptotically stable under temporal perturbation if  $\beta > \beta_h$ . However, the same equilibrium may become unstable due to spatial perturbation. This phenomenon is called Turing instability. The other spatially homogeneous solution of system (10) corresponding to  $P_2^*$  cannot be Turing unstable as it is a saddle point and hence always unstable under temporal perturbation. Therefore, we derive the conditions for Turing instability of the homogeneous steady-state solution corresponding

to equilibrium point  $P_1^* = (S^*, I_1^*)$ . Consider spatio-temporal perturbation around  $P_1^*$  as

$$\begin{aligned} S &= S^* + \epsilon S_1 e^{\lambda t + ikx}, \quad I = I_1^* + \epsilon I_1 e^{\lambda t + ikx}, \\ \text{where } |\epsilon| &\ll 1 \text{ and } k = \frac{n\pi}{L} \text{ is the wavenumber. After substituting these into system (10) and linearizing, we find} \\ \mathcal{J}_k \begin{pmatrix} S_1 \\ I_1 \end{pmatrix} &\equiv \begin{pmatrix} a_{11} - d_1 k^2 & a_{12} \\ a_{21} & a_{22} - d_2 k^2 \end{pmatrix} \begin{pmatrix} S_1 \\ I_1 \end{pmatrix} \\ &= \begin{pmatrix} 0 \\ 0 \end{pmatrix}. \end{aligned} \quad (11)$$

The characteristic equation of the matrix  $\mathcal{J}_k$  in (11) is  $\lambda^2 - \mathcal{B}(k^2)\lambda + \mathcal{C}(k^2) = 0$ , (12)

where

$$\mathcal{B}(k^2) = \text{Trace}(\mathcal{J})|_{P_1^*} - (d_1 + d_2)k^2 \text{ and}$$

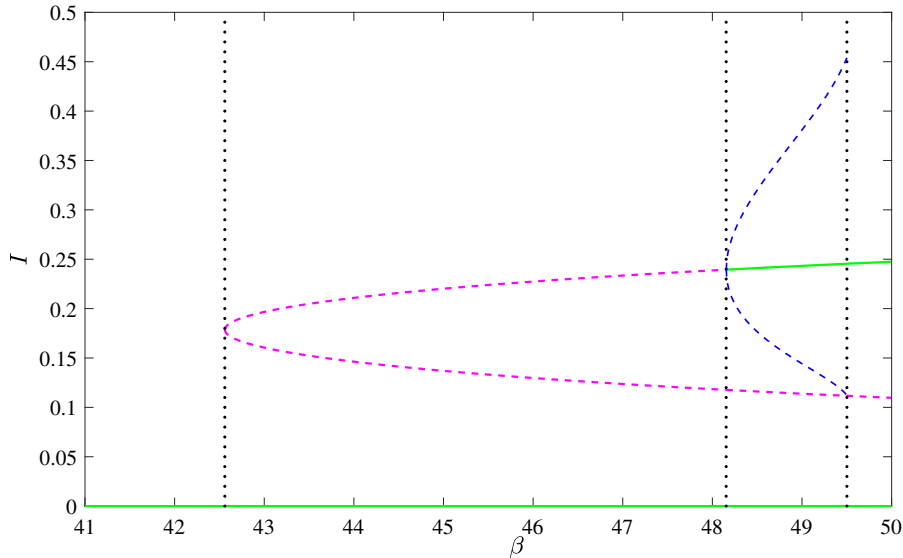


**Fig. 2** One parameter bifurcation diagram with respect to the parameter  $\beta$ . The dashed magenta curve depicts unstable endemic equilibria that appear due to a saddle-node bifurcation at  $\beta = \beta_c \approx 42.56$ . The dashed blue curve represents an unstable limit cycle that appears due to a subcritical Hopf bifurcation at  $\beta = \beta_h \approx 48.39$ . Further, the solid green curves represent

a stable disease-free equilibrium in the bottom axis and a stable endemic equilibrium post-Hopf bifurcation at  $\beta = \beta_h$ . Finally, the unstable limit cycle disappears through a homoclinic bifurcation at  $\beta \approx 49.50$ . Other parameter values are given in the caption of Fig. 1

$$\mathcal{C}(k^2) = \text{Det}(\mathcal{J})|_{P_1^*} - (a_{11}d_2 + a_{22}d_1)k^2 + d_1d_2k^4. \quad (13)$$

For stability of the spatially homogeneous steady state, we must have  $\mathcal{B}(k^2) < 0$  and  $\mathcal{C}(k^2) > 0$  for all  $k > 0$ . However, violation of any one of these two leads to instability of the homogeneous steady state. It may be noted that  $\mathcal{B}(k^2) < 0$  for all  $k > 0$ . Hence, the condition of Turing instability reduces to  $\mathcal{C}(k^2) < 0$  for some  $k$ . Now, the minimum value of  $\mathcal{C}(k^2)$  is

$$\mathcal{C}_{\min}(k^2) = \text{Det}(\mathcal{J})|_{P_1^*} - \frac{(a_{11}d_2 + a_{22}d_1)^2}{4d_1d_2}, \quad (14)$$

which is attained at  $k^2 = (a_{11}d_2 + a_{22}d_1)/2d_1d_2$ . Since  $k^2$  is a real positive, this is feasible only when  $a_{11}d_2 + a_{22}d_1 > 0$ . Also, since  $\mathcal{C}_{\min}(k^2) < 0$ , we must have

$$a_{11}d_2 + a_{22}d_1 > 2\sqrt{d_1d_2 \text{Det}(\mathcal{J})|_{P_1^*}}.$$

Hence, the Turing bifurcation threshold is obtained when  $\mathcal{C}_{\min}(k^2) = 0$  at critical wavenumber  $k = k_c$  and the corresponding critical value of  $d_1$ , denoted by  $d_1^c$ , is

$$d_1^c = \frac{d_2}{a_{22}^2} [(a_{11}a_{22} - 2a_{12}a_{21}) + \sqrt{(a_{11}a_{22} - 2a_{12}a_{21})^2 - a_{22}^2a_{11}^2}]. \quad (15)$$

If  $d_1 > d_1^c$ , then  $\mathcal{C}_{\min}(k^2) < 0$  whenever  $k \in (k_-, k_+)$ , and the boundaries of the interval are obtained by solving  $\mathcal{C}(k^2) = 0$ :

$$k_- = \sqrt{\frac{a_{11}d_2 + a_{22}d_1 - \mathcal{D}}{2d_1d_2}} \quad \text{and} \quad k_+ = \sqrt{\frac{a_{11}d_2 + a_{22}d_1 + \mathcal{D}}{2d_1d_2}}, \quad (16)$$

where

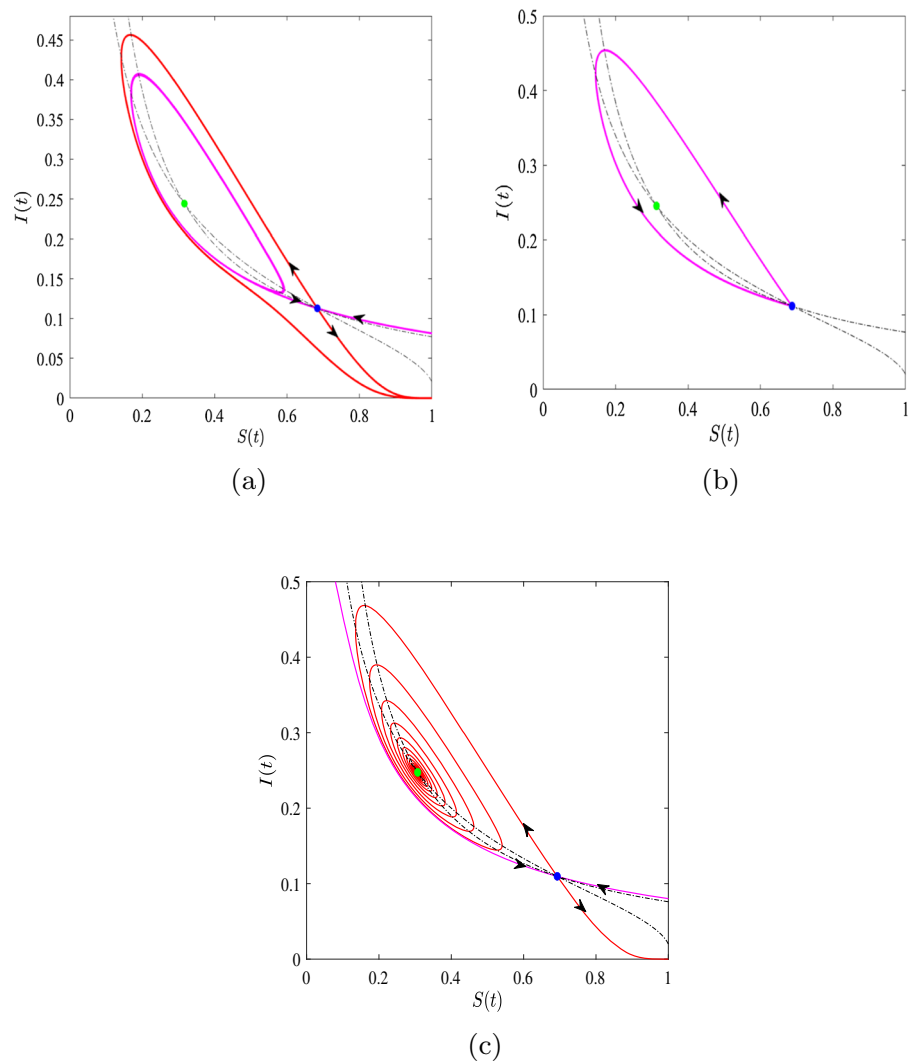
$\mathcal{D} = \sqrt{(a_{11}d_1 + a_{22}d_2)^2 - 4d_1d_2(a_{11}a_{22} - a_{21}a_{12})}$ . Thus, system (10) is Turing unstable for a range of wavenumber lying in the interval  $(k_-, k_+)$  whenever  $d_1 > d_1^c$ . A solution with wavenumber  $k_n = \frac{n\pi}{L}$ , called an  $n$ -mode solution, is Turing unstable for  $d_1 > d_1^c$ , if the domain size  $L$  lies in the interval  $(L_-^n, L_+^n)$ , where

$$L_-^n = \frac{n\pi}{k_+} \quad \text{and} \quad L_+^n = \frac{n\pi}{k_-}. \quad (17)$$

## 5 The nonlocal spatio-temporal model

It has been observed that the transmission of diseases is not limited to the spatial location of infected species,

**Fig. 3** Phase portraits of the temporal system (1) for different values of the bifurcation parameter  $\beta$ : **a** persistence of the unstable limit cycle at  $\beta = 49.2 > \beta_h$ , **b** homoclinic loop at  $\beta = 49.5$ , and **c** phase portrait at  $\beta = 50$ . These plots show the emergence of the unstable limit cycle through a subcritical Hopf bifurcation at  $\beta = \beta_h$ , and the same disappears in the homoclinic loop bifurcation. In panel (c), the stable manifold of the saddle point  $P_2^*$  (magenta-colored curve) serves as the separatrix between the basins of attraction of the attractors  $P_1^*$  and  $P_0$ . Other parameter values are given in the caption of Fig. 1.



rather the phenomenon is spatially nonlocal in the sense that a susceptible individual is at risk of acquiring infection in a vicinity of an infected individual. Moreover, the chances of infection depend on the spatial distance of a susceptible from an infected. Generally, a weighted average of the population around an infected is assumed to derive the nonlocal term, which results in a convolution integral with a specified non-negative kernel function describing the weightage. Therefore, the force of infection for our model system is modified as

$$\begin{aligned} \lambda(x, t; I) &= (\Psi_\delta * I^2)(x, t) \\ &= \beta \int_{-\infty}^{\infty} \Psi_\delta(x - y) I^2(y, t) dy, \end{aligned} \quad (18)$$

where  $\Psi_\delta(x - y)$  is a non-negative kernel function, which quantifies the influence of the infected present

at location  $y$  in the neighborhood of the location  $x$ . It is assumed that the influence of the neighboring infected individuals on disease transmission becomes negligible for large enough spatial distances and spatially symmetric:

$$\Psi_\delta(x) \rightarrow 0 \text{ as } x \rightarrow \infty \text{ and } \Psi_\delta(-x) = \Psi_\delta(x).$$

In our model system, we assume that the nonlocal infection is restricted within a length of  $2\delta$  around any spatial point  $x$  and it is uniformly distributed, i.e.,

$$\Psi_\delta(x) = \begin{cases} \frac{1}{2\delta} & \text{if } |x| \leq \delta, \\ 0 & \text{otherwise,} \end{cases} \quad (19)$$

where  $\delta > 0$  measures the extent of the nonlocal disease transmission. Therefore, the local model (10) can

be modified to a nonlocal model incorporating the distance disease transmission:

$$\begin{aligned}\frac{\partial S}{\partial t} &= \Lambda - \lambda(x, t; I)S + \gamma I - \mu S + d_1 \frac{\partial^2 S}{\partial x^2}, \\ \frac{\partial I}{\partial t} &= \lambda(x, t; I)S - (\gamma + \sigma + \mu)I + d_2 \frac{\partial^2 I}{\partial x^2},\end{aligned}\quad (20)$$

where  $d_1$  and  $d_2$  are two non-negative constants accounting for the diffusion coefficients corresponding to the susceptible and infected population. One may observe that  $\int_{-\infty}^{\infty} \Psi_\delta(s)ds = 1$ , which signifies that the nonlocal system (20) admits the same spatially homogeneous steady states as that of the corresponding local system (10). Finally, one may note that the nonlocal model (20) reduces to the local model (10) as  $\delta \rightarrow 0$ .

### 5.1 Linear stability analysis

Model (20) possesses three spatially homogeneous steady-state solutions corresponding to the three equilibria of the temporal model (1). Again, linearizing the nonlocal model (20) around the homogeneous steady-state solution corresponding to equilibrium  $P_1^*$  by introducing the same spatio-temporal perturbation used for the local diffusion model (10), we get

$$\begin{aligned}\mathcal{J}_N \begin{pmatrix} S_1 \\ I_1 \end{pmatrix} \\ \equiv \begin{pmatrix} a_{11} - d_1 k^2 & -2\beta S^* I_1^* \widehat{\Psi}_\delta(k) + \gamma, \\ a_{21} & 2\beta S^* I_1^* \widehat{\Psi}_\delta(k) - (\gamma + \sigma + \mu) - d_2 k^2 \end{pmatrix} \\ \begin{pmatrix} S_1 \\ I_1 \end{pmatrix} = \begin{pmatrix} 0 \\ 0 \end{pmatrix}.\end{aligned}\quad (21)$$

Here,  $a_{11}$ ,  $a_{21}$  are the same as given earlier and  $\widehat{\Psi}_\delta(k)$  denotes the Fourier transform of the kernel step function:

$$\widehat{\Psi}_\delta(k) := \int_{-\infty}^{\infty} \Psi_\delta(z) e^{-ikz} dz = \frac{\sin k\delta}{k\delta}. \quad (22)$$

The characteristic equation of the matrix  $\mathcal{J}_N$  becomes

$$\eta^2 - \tilde{\mathcal{B}}(\delta, k)\eta + \tilde{\mathcal{C}}(\delta, k) = 0, \quad (23)$$

where

$$\begin{aligned}\tilde{\mathcal{B}}(\delta, k) &= a_{11} + 2\beta S^* I_1^* \frac{\sin k\delta}{k\delta} \\ &\quad - (\gamma + \sigma + \mu) - (d_1 + d_2)k^2\end{aligned}\quad (24)$$

and

$$\begin{aligned}\tilde{\mathcal{C}}(\delta, k) &= d_1 d_2 k^4 - \left[ \{2\beta S^* I_1^* \frac{\sin k\delta}{k\delta} \right. \\ &\quad \left. - (\gamma + \sigma + \mu)\} d_1 + a_{11} d_2 \right] k^2 \\ &\quad + 2(a_{11} + a_{21})\beta S^* I_1^* \frac{\sin k\delta}{k\delta} \\ &\quad - (\gamma + \sigma + \mu)a_{11} - a_{21}\gamma\end{aligned}\quad (25)$$

are the trace and determinant of the Jacobian matrix  $\mathcal{J}_N$  given in (21). For a fixed  $\delta$ , the homogeneous steady-state solution, corresponding to  $P_1^*$ , of the nonlocal model (20) is locally asymptotically stable if  $\tilde{\mathcal{B}}(\delta, k) < 0$  and  $\tilde{\mathcal{C}}(\delta, k) > 0$  hold for all  $k > 0$ . Our particular interest is to find out the conditions for which the homogeneous steady state becomes unstable. In other words, at least one of the above inequalities does not hold for a particular choice of  $k$  and  $\delta$ .

**Proposition 6** *The nonlocal system (20) does not undergo spatial Hopf bifurcation.*

*Proof* To prove this, we show that the trace of the Jacobian matrix  $\mathcal{J}_N$  remains negative for any  $k, \delta > 0$ , whenever the steady state  $P_1^*$  of the temporal system (1) is stable. Note that the first equation of (2) yields

$$\beta S^* I_1^* = \gamma + \sigma + \mu.$$

After some algebraic manipulation, the trace of the matrix  $\mathcal{J}_N$  can be written as

$$\begin{aligned}\tilde{\mathcal{B}}(\delta, k) &= -\beta(I_1^*)^2 + (\sigma + \gamma) - 2(\gamma + \sigma + \mu) \\ &\quad \left(1 - \frac{\sin k\delta}{k\delta}\right) - (d_1 + d_2)k^2.\end{aligned}\quad (26)$$

Since the steady state  $P_1^*$  of the temporal model (1) is stable, the trace of the corresponding Jacobian matrix  $\mathcal{J}$  in (5) must be negative, i.e.,

$$\text{Trace}(\mathcal{J}) = a_{11} + a_{22} = (\sigma + \gamma) - \beta(I_1^*)^2 < 0.$$

Again, it is known that  $\frac{\sin t}{t} < 1$  for all  $t > 0$ . Hence, the proposition follows from (26).  $\square$

Therefore, for a fixed  $\delta$ , the homogeneous steady-state corresponding to  $P_1^*$  losses its stability only when  $\tilde{\mathcal{C}}(\delta, k) < 0$  for some  $k > 0$ . This leads to Turing instability for the nonlocal system (20). It is observed from (25) that  $\tilde{\mathcal{C}}(\delta, k) > 0$  as  $k \rightarrow 0$  and  $k \rightarrow \infty$ . For Turing instability, we must have  $\tilde{\mathcal{C}}(\delta, k) < 0$  for some  $k$  associated with a fixed  $\delta$ . Suppose that  $\tilde{\mathcal{C}}$  attains a local

minimum 0 for a unique wavenumber  $k = k_T > 0$  at the critical value  $d_1 = d_1^T$ , which gives

$$\tilde{C}(\delta, k_T) = 0 \text{ and } \frac{\partial \tilde{C}}{\partial k}(\delta, k_T) = 0 \quad \text{for some fixed } \delta. \quad (27)$$

Solution of the first equation of (27) gives the critical value  $d_1$  as

$$d_1^T = \frac{a_{11}d_2k_T^2 - 2(a_{11} + a_{21})\beta S^* I_1^* \frac{\sin k_T \delta}{k_T \delta} + (\gamma + \sigma + \mu)a_{11} + \gamma a_{21}}{k_T^2 \{d_2k_T^2 - 2\beta S^* I_1^* \frac{\sin k_T \delta}{k_T \delta} + (\gamma + \sigma + \mu)\}}. \quad (28)$$

Substituting  $d_1^T$  into the second equation of (27), we get

$$\begin{aligned} & \left[ 2d_2k_T^2 - \beta S^* I_1^* \left( \cos k_T \delta + \frac{\sin k_T \delta}{k_T \delta} \right) \right. \\ & + (\gamma + \sigma + \mu) \left. \right] \\ & \times \left[ a_{11}d_2k_T^2 - 2(a_{11} + a_{21})\beta S^* I_1^* \frac{\sin k_T \delta}{k_T \delta} \right. \\ & + (\gamma + \sigma + \mu)a_{11} + \gamma a_{21} \left. \right] \\ & - \left( d_2k_T^2 - 2\beta S^* I_1^* \frac{\sin k_T \delta}{k_T \delta} + \gamma + \sigma + \mu \right) \\ & \times \left[ a_{11}d_2k_T^2 - (a_{11} + a_{21})\beta S^* I_1^* \right. \\ & \left. \left( \cos k_T \delta - \frac{\sin k_T \delta}{k_T \delta} \right) \right] = 0. \end{aligned} \quad (29)$$

The last equation is a transcendental equation in  $k_T$  which is solved by a numerical root-finding technique. The calculated value of  $k_T$  is then substituted into (28) to find the critical diffusion coefficient  $d_1^T$ . Furthermore, corresponding to a fixed  $\delta$ , it is observed that  $\tilde{C}(\delta, k_T) < 0$  whenever  $d_1 > d_1^T$  for a range of values of  $k$ . Let us denote the minimum value of  $\tilde{C}$  by  $\tilde{C}_{\min}$ . System (20) undergoes Turing bifurcation when  $\tilde{B} < 0$  and  $\tilde{C}_{\min} = 0$ . The curve corresponding to  $\tilde{C}_{\min} = 0$  is called Turing curve, and the portion on this curve satisfying  $\tilde{B} < 0$  is called Turing bifurcation curve.

## 6 Numerical results

Here, we present various spatio-temporal patterns exhibited by both the local and nonlocal spatial models. The governing equations with periodic boundary conditions are discretized using the central difference formula for space and forward Euler method for the time. The nonlocal terms of system (20) are integrated using

the composite trapezoidal rule. Also, pulse-type initial conditions around the endemic point  $P_1^*$  are taken:

$$S(x, 0) = \begin{cases} S^* + \nu & \text{for } |x| \leq 10, \\ 0 & \text{Otherwise,} \end{cases} \quad (30)$$

$$\text{and } I(x, 0) = \begin{cases} I_1^* + \nu & \text{for } |x| \leq 10, \\ 0 & \text{Otherwise,} \end{cases}$$

where  $|\nu| \ll 1$ . In our simulations, we take  $L = 50$ , mesh spacing  $h = 0.2$  and time step  $\tau = 10^{-3}$ . We verified that these mesh sizes are small enough not to bring numerical artifacts. We keep parameters  $\Lambda = 1$ ,  $\mu = 1$ ,  $\sigma = 1.8$ ,  $\gamma = 1$ ,  $d_2 = 1$  fixed and vary the parameters  $\beta$ ,  $d = d_1$  in admissible ranges. Numerical solutions of both the local and nonlocal systems are presented using various color plots of the infected population only since there is significant cross-correlation between the spatial distribution of the susceptible and that of the infected population.

### 6.1 Patterns: local infection model

Turing instability condition (15) along with temporal Hopf threshold divides the  $(\beta, d)$  parameter plane into stable, Turing, Turing–Hopf, and Hopf domains shown in Fig. 4. The solution characteristics for various representative points in each region are also marked in Fig. 4. A stationary in time but heterogeneous in space Turing pattern, exhibited by system (10) for a representative point in the Turing domain, is shown in Fig. 5a. This kind of pattern emerges in the biological system due to the self-organization of individuals through numerous interactions. Figure 5b depicts the spatial distribution of both the susceptible and infected populations in the final steady state. A similar pattern can also be observed for some representative points taken from the Turing–Hopf domain. However, oscillatory solutions can also be observed in this domain with the dispersal rate  $d$  close to the Turing curve. The stable domain gives the spatially homogeneous endemic solution corresponding to  $P_1^*$ . System (10) possesses quasi-periodic and chaotic spatio-temporal solutions in the Hopf domain. However, this domain also contains disease-free spatially homogeneous solutions for smaller values of both  $\beta$  and  $d$ . Hence, in the parametric regime marked with “\*” in Fig. 4, both the temporal model and corresponding spatio-temporal model produce stable disease-free homogeneous solutions. It is observed that the hetero-

**Fig. 4** Representative solutions in the  $(\beta, d)$  parametric plane for the local system (10). Here, solid blue and black dashed curves represent Turing and temporal Hopf curves, respectively. Further, +, o, \*, and  $\Delta$  correspond to non-homogeneous stationary, oscillatory (chaotic or quasi-periodic), stationary homogeneous disease-free, and stationary homogeneous endemic solutions. Other parameter values are  $\Lambda = 1$ ,  $\mu = 1$ ,  $\sigma = 1.8$ ,  $\gamma = 1$ , and  $d_2 = 1$

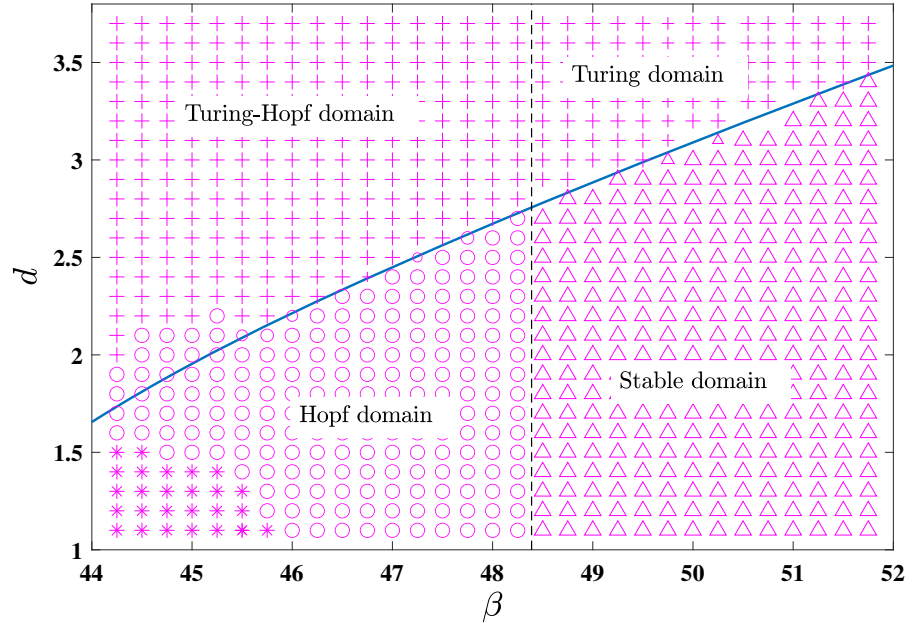
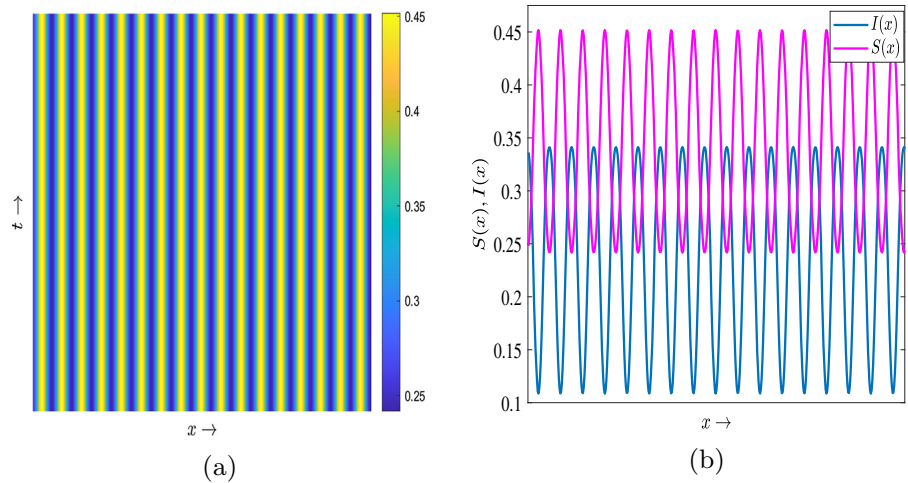


**Fig. 5** Distribution of populations in the Turing domain for the choice  $\beta = 48.5$  and  $d = 3 : \mathbf{a}$  Turing pattern for the infected population in space-time plane,  $\mathbf{b}$  spatial distribution of both the susceptible and infected populations. Other parameter values are given in the caption of Fig. 4



geneous population densities oscillate with time initially, but a sudden change is observed that causes system (10) to stabilize in the disease-free state. Further, the duration of the initial oscillation depends upon the choice of parameters and initial condition.

The number of stationary patches in the Turing pattern can be explained, and it depends on the size of the domain. In Fig. 5, the infected population  $I(x, t)$  is stationary in time but periodic in space. If  $k_m$  is the wavenumber lying in  $(k_-, k_+)$  with maximum growth rate, then the associated wavelength of the solution is  $w_m = \frac{2\pi}{k_m}$ . This is illustrated by the dispersion relation plot in Fig. 6 for the Turing pattern shown in Fig. 5.

Here, the wavenumber corresponding to the dominated unstable eigenmode  $k_m \approx 1.07$  is marked with a large blue asterisk in Fig. 6. Therefore, the corresponding wavelength  $w_m \approx 5.87$  and the number of stationary patches in the Turing pattern is  $\frac{2L}{w_m} \approx 17$ . This is in agreement with Fig. 5.

On the other hand, if we chose a representative point from the Hopf domain depicted in Fig. 4, then the system exhibits various kinds of dynamical patterns. The associated phase diagrams of spatially averaged densities of susceptible and infected populations, denoted by  $\langle S \rangle$  and  $\langle I \rangle$ , are used to characterize these patterns. Some of these interesting patterns with corresponding

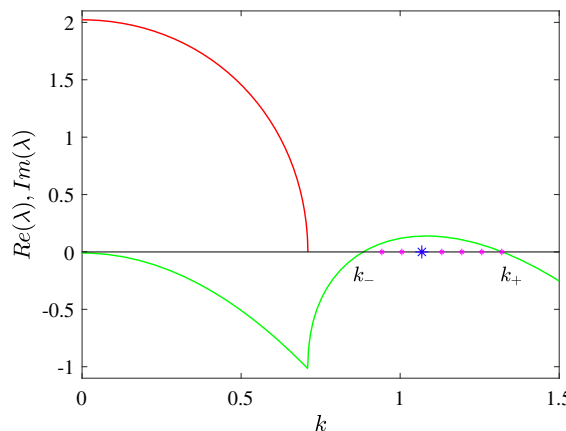


**Fig. 6** Dispersion relation for the local system (10) corresponding to  $d = 3$  and  $\beta = 48.5$ . Green and red curves represent the real and imaginary parts of the eigenvalues against wavenumber  $k$ . The asterisks denote the wavenumbers corresponding to the unstable eigenmodes lying in  $(k_-, k_+)$ , and the large blue asterisk represents the wavenumber of the most unstable eigenmode. Other parameter values are given in the caption of Fig. 4

phase diagrams of the spatially averaged population are shown in Fig. 7. Here, we fixed  $\beta = 47.5$  and varied  $d$  in the admissible range. First, we take the value of  $d$  to be 1, that is, when both the susceptible and infected populations can disperse at equal rates in the domain. Figure 7a displays the space-time pattern of the infected population of the system, and the associated phase portrait of the spatial averages of the populations is presented in Fig. 7b. The phase portrait depicts the chaotic nature of the solution. Further, we increase the value of  $d$  to 2.4 which is near the Turing curve. For this choice of parameters, Fig. 7c displays the space-time pattern of the infected population and the associated phase portrait of the spatial averages of the populations is shown in Fig. 7d. Though both the cases of  $d = 1$  and  $d = 2.4$  give spatio-temporal chaos, there are qualitative differences evident from the associated plots. In particular, as we gradually increase  $d$ , the frequency of the irregular oscillations decreases but the amplitude increases. This leads to the occurrence of triangle-shaped structures in the pattern shown in Fig. 7c. If we further increase  $d$ , then parameter values cross the Turing curve into the Turing–Hopf region and the temporal oscillations disappear. In search of diverse dynamic patterns in the Hopf domain, we next choose  $\beta = 46$  and  $d = 2$ . Figure 8a, b shows the space-time pattern of the infected class and the phase diagram of the spatial averages of the populations. A close look at

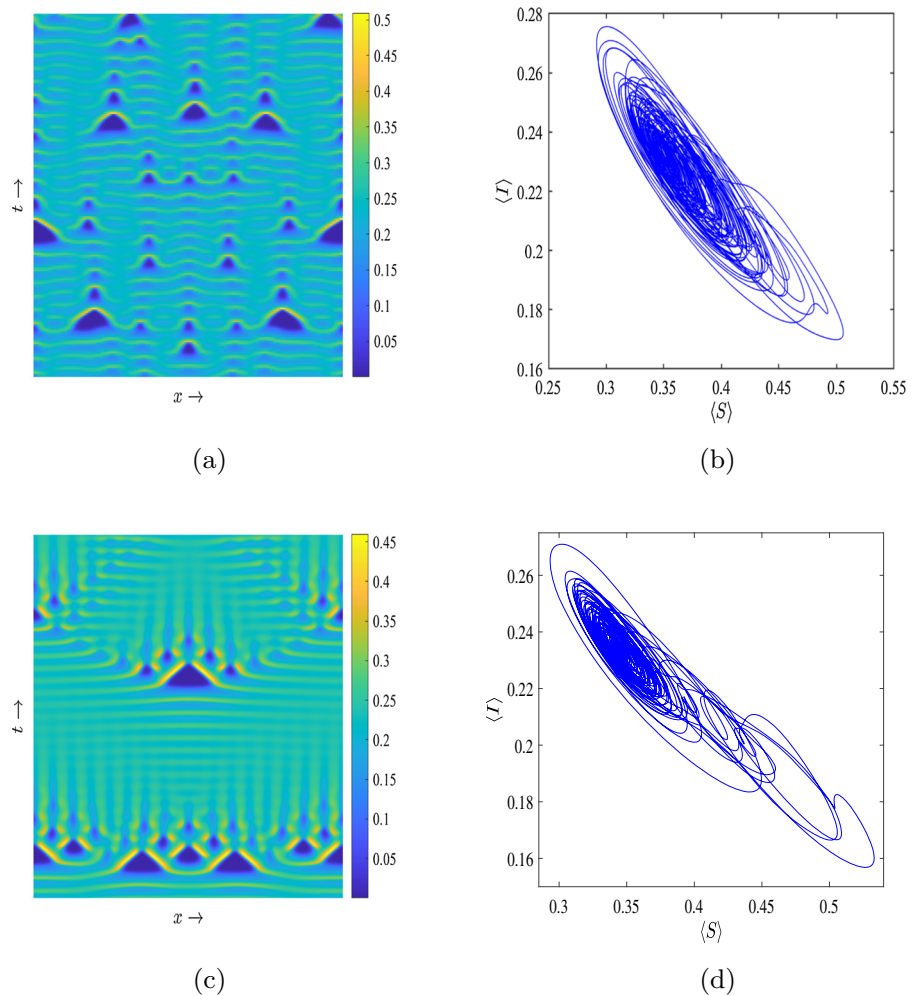
Fig. 8a reveals that the pattern is not periodic in space–time scale; however, the annulus-shaped structure of the spatially averaged phase diagram plotted in Fig. 8b suggests the quasi-periodic nature of the patterns.

## 6.2 Patterns: nonlocal infection model

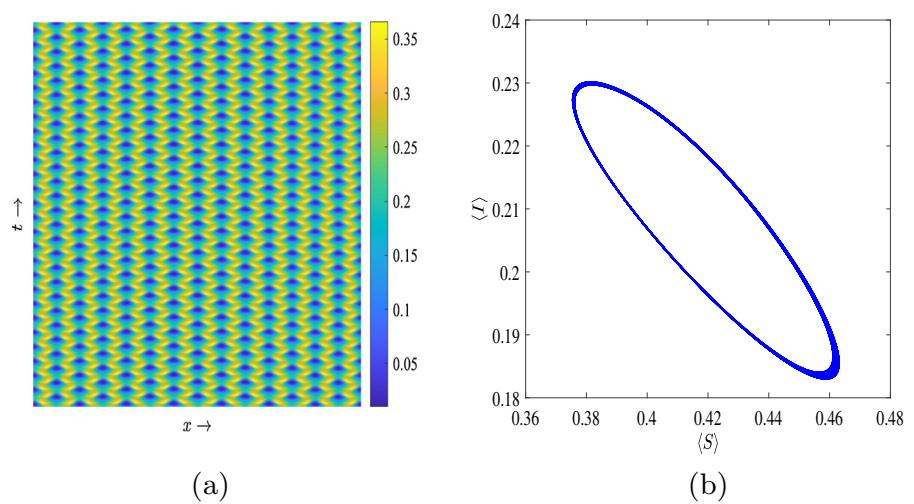
In this subsection, the solutions of the nonlocal model (20) are investigated numerically. First, we investigate the effects of the extent of nonlocal disease transmission parameter,  $\delta$ , on the Turing curve. For this purpose, we solve (29) numerically for  $k_T$  and substitute it in (28) to find the Turing curve in the  $(\beta, d)$  plane. A few of these curves, for different values of  $\delta$ , are plotted in Fig. 9a. Clearly, Turing curves for the nonlocal model approach that of the local model as  $\delta \rightarrow 0+$ . It is seen from Fig. 9a that a Turing curve shifts upward with an increase in the parameter  $\delta$ . Similar to the local model, the Turing curve along with the temporal Hopf threshold divide the  $(\beta, d)$  parameter plane into stable, Turing, Turing–Hopf, and Hopf domains. However, one may note that Hopf and stable domains enlarge compared to that of the local model (10) with a gradual increase of  $\delta$ . Solution characteristics in each region are qualitatively similar to that of the local model as depicted in Fig. 9b for  $\delta = 0.6$ . However, the homogeneous disease-free solutions appear in a larger region which also overlaps with the Turing–Hopf domain for  $\delta = 0.6$ . This leads to the shrinking of the region for the oscillatory (chaotic or quasi-periodic) solutions. It is observed that the region of the disease-free solutions increases with an increase in  $\delta$ . It is also observed that the enlargement of the region possessing spatially homogeneous disease-free steady state is proportional to the value of  $\delta$ . Thus, a larger value of  $\delta$  further increases the stabilized region in the Hopf domain. Now, we discuss solution characteristics for some representative points from Fig. 9b.

First, we fixed  $\beta = 47.5$  and  $d = 2.8$  and examined the effects of the nonlocal disease transmission on the spatio-temporal patterns by varying the parameter  $\delta$ . For the local model, i.e.,  $\delta = 0$ , the above parameters lie in the Turing–Hopf domain which leads to a stationary Turing pattern. Next, we choose three different values of  $\delta$  and the corresponding spatio-temporal plots are shown in Figs. 10 and 11. For all the three values of  $\delta$ , the parameter values  $\beta = 47.5$  and  $d = 2.8$  lie in the Hopf domain of the nonlocal model, and the distances

**Fig. 7** Spatio-temporal plots of the local system (10) corresponding to  $\beta = 47.5$  for  $d = 1$  **a, b** and  $d = 2.4$  **c, d**. Space-time patterns are shown in **(a, c)**; and phase diagrams of the spatially averaged populations are shown in **(b, d)**. Other parameter values are given in the caption of Fig. 4. These plots show spatio-temporal chaotic dynamics of the local system (10) in the Hopf domain



**Fig. 8** Spatio-temporal plots corresponding to  $\beta = 46$ ,  $d = 2$ : **a** quasi-periodic pattern exhibited by the infected population, **b** phase diagram of the spatially averaged populations. Other parameter values are given in the caption of Fig. 4. These plots show quasi-periodic dynamics of the local system (10) in the Hopf domain



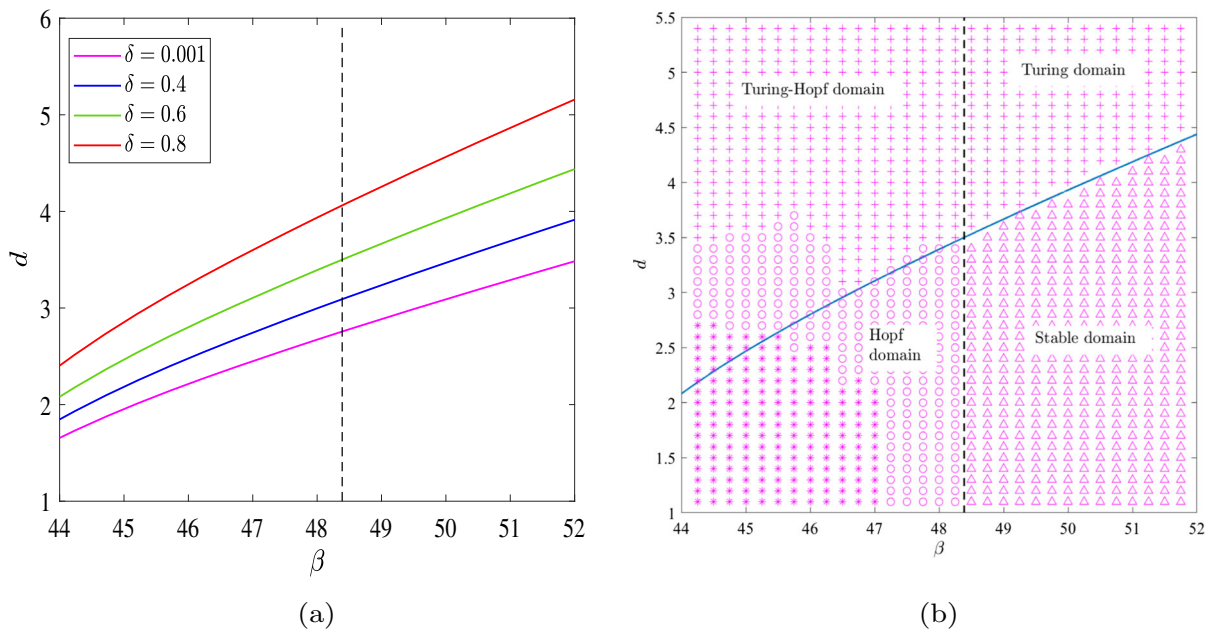


**Fig. 9** Spatio-temporal solutions of nonlocal model: **a** Turing bifurcation curves are plotted together with the temporal Hopf curve (black vertical dashed line) for different values  $\delta$ , **b** regions of stationary and oscillatory solutions in the  $(\beta, d)$  parametric plane obtained from numerical simulation of system (20) for  $\delta = 0.6$ . Here, the solution characteristics marked

with +,  $\circ$ ,  $*$ , and  $\Delta$  correspond to non-homogeneous stationary, oscillatory (chaotic or quasi-periodic), stationary homogeneous disease-free, and stationary homogeneous endemic solutions. Other parameter values are  $\Lambda = 1$ ,  $\mu = 1$ ,  $\sigma = 1.8$ ,  $\gamma = 1$ , and  $d_2 = 1$ . As  $\delta$  increases, Turing and Turing-Hopf regions shrink but those of Hopf and homogeneous stable expand

of the point from the Turing curve increase with  $\delta$ . Figure 10b, d describes the chaotic nature of the patterns for  $\delta = 0.4$  and  $0.8$ . However, there are some qualitative changes that can be observed between  $\delta = 0.4$  and  $\delta = 0.8$  cases. First, the spatial averages of both the populations oscillate with higher frequency in the case of  $\delta = 0.8$ . Second, the triangle-shaped structures become smaller and more in number in Fig. 10c. It is noted that the frequency of the spatially averaged population increases as we go away from the Turing curve in the Hopf region. The point representing  $\beta = 47.5$  and  $d = 2.8$  lies further away from the Turing curve for  $\delta = 0.8$  than  $\delta = 0.4$ . However, further increment in  $\delta$  makes the same point more distant from the Turing curve and the chaotic nature of the spatio-temporal pattern disappears. For example, the spatio-temporal pattern and phase diagram for  $\delta = 1.0$  shown in Fig. 11a, b confirm the less chaotic nature of the pattern.

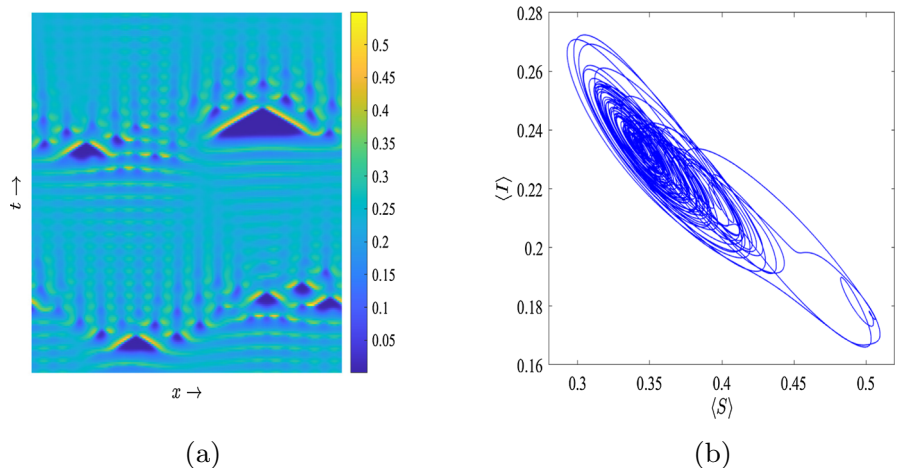
We also examine the effects of the nonlocal extent of the disease transmission  $\delta$  on the number of stationary patches observed in Turing patterns of system (20). For this, we fix  $\beta = 48.5$  and  $d = 10$ , which lie in the pure

Turing domain for  $0 \leq \delta \leq 1$ . The critical wavenumber for the local model ( $\delta = 0$ ) is  $k_c \approx 0.87965$ , and hence, the wavelength of each patch is  $w_c = \frac{2\pi}{k_c} \approx 7.14282$ . Thus, the number of stationary patches is  $L/w_c \approx 14$ , which matches with our simulation result shown in Fig. 12 for  $\delta = 0$ . The number of stationary patches of the Turing pattern decreases gradually with an increase in  $\delta$  as shown in Fig. 12. Thus, we conclude that the wavelength increases with increments in  $\delta$ . One possible explanation of this phenomenon from the epidemiological point of view is that the patch sizes for the infected and susceptible increase with an increase in the extent to transmit the disease. This leads to fewer patches in a given domain size for a higher value of  $\delta$ .

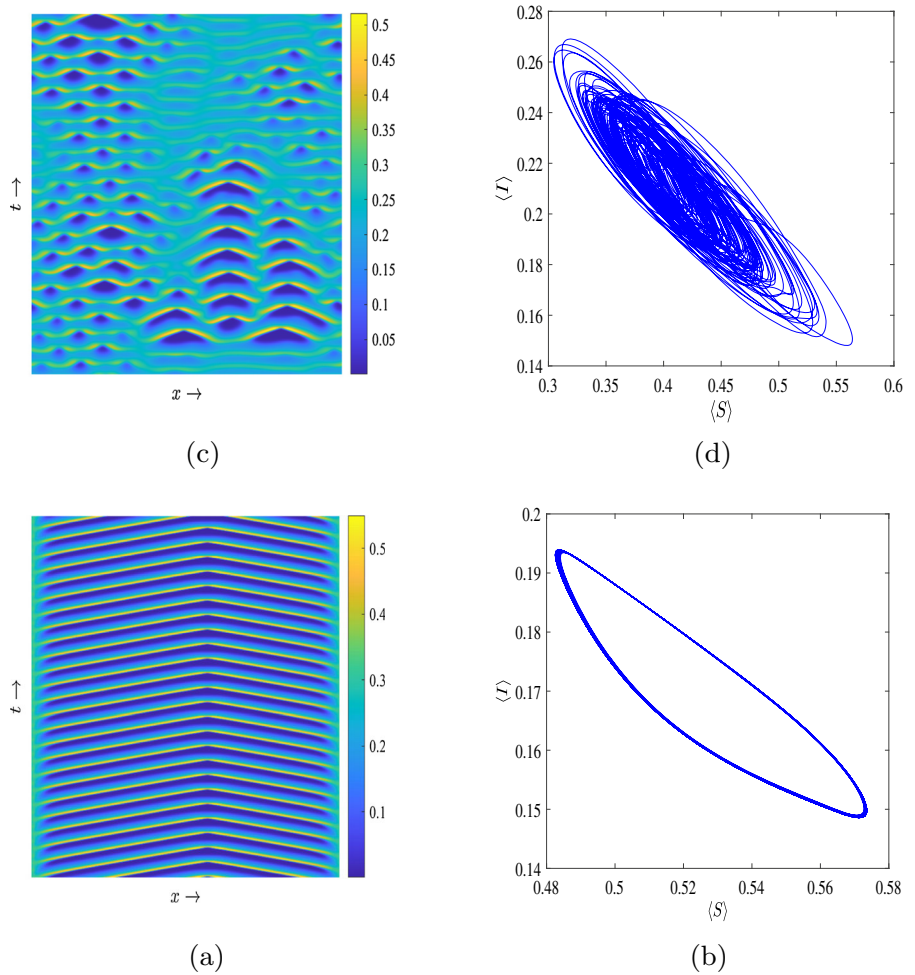
### 6.3 Transient dynamics of the spatio-temporal models

Analysis of transition dynamics is critical to an epidemic model and plays a vital role in making disease mitigation policies. In this study, we investigate the transient dynamics of both the local and nonlocal sys-

**Fig. 10** Spatio-temporal plots of the nonlocal system (20) corresponding to  $\beta = 47.5$  and  $d = 2.8$  with the initial condition (30) for  $\delta = 0.4$  (a, b) and  $\delta = 0.8$  (c, d). Space–time patterns are shown in a and c, and phase diagrams of the spatially averaged populations are shown in b and d. Other parameter values are given in the caption of Fig. 9. These plots show spatio-temporal chaotic dynamics of the nonlocal system (20) in the Hopf domain



**Fig. 11** Spatio-temporal plots of the nonlocal system (20) corresponding to  $\beta = 47.5$  and  $d = 2.8$  with the initial condition (30)  $\delta = 1.0$ . Space–time pattern is shown in (a), and phase diagram of the spatially averaged populations is shown in (b). Other parameter values are given in the caption of Fig. 9. These plots show quasi-periodic dynamics of the nonlocal system (20) in the Hopf domain



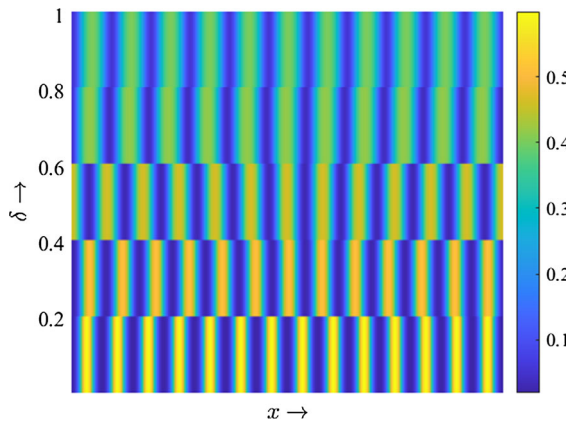


**Fig. 12** Colored plots of the stationary patterns of the nonlocal system (20) for the infected population starting with initial condition (30). Here,  $\delta$  is varied from 0 to 1 keeping  $\beta = 48.5$  and  $d = 10$  fixed. Other parameter values are given in the caption of Fig. 9. The plot shows that the number of stationary patches decreases with an increment in  $\delta$

tems with the help of numerical simulations. We choose the following initial condition:

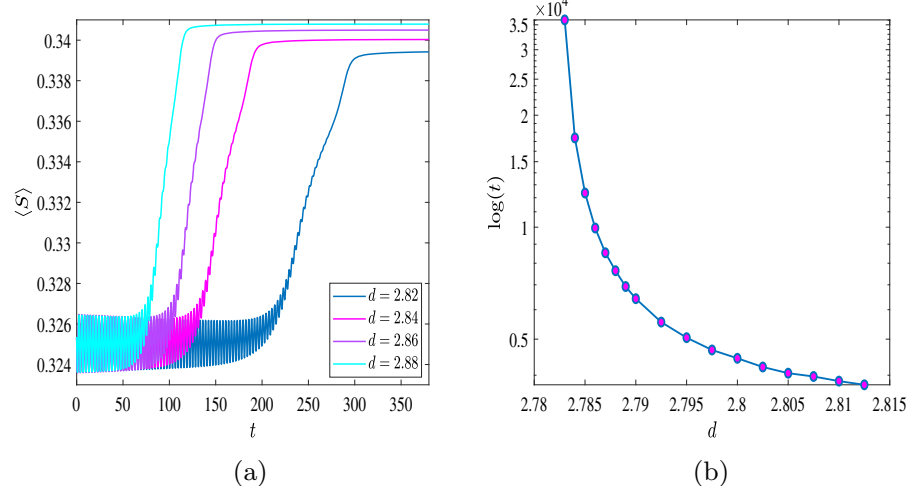
$$S(x, 0) = \begin{cases} S^* + \nu & \text{for } |x| \leq 10, \\ 0 & \text{Otherwise,} \end{cases}$$

and  $I(x, 0) = \begin{cases} I_1^* + \nu & \text{for } |x| \leq 10, \\ 0 & \text{Otherwise,} \end{cases}$  (31)

where  $\nu = 10^{-2}$ .

The local system (10) exhibits stationary Turing patterns in the Turing domain whenever  $d > d_1^c$  for a fixed value of  $\beta$ . We choose  $\beta = 48.5$  for which the corresponding  $d_1^c \approx 2.78$ . We are primarily concerned with

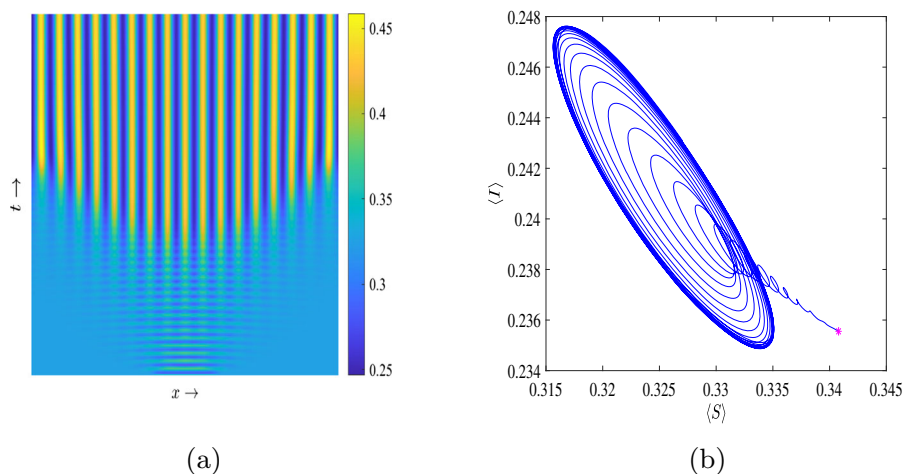
**Fig. 13** Transient dynamics of the local model (10) for  $\beta = 48.5$ : **a** temporal evolution of the spatially averaged susceptible population for different dispersal rate and **b** plot of transient time duration in the logarithmic scale against  $d$ . Other parameter values are  $\Lambda = 1$ ,  $\mu = 1$ ,  $\sigma = 1.8$ ,  $\gamma = 1$ , and  $d_2 = 1$



the time duration spent on the transient state before reaching the stationary state and the transient patterns observed in the system. The dependence of the duration of the transient period on the spatial dispersal rate can be found in [36]. Here, we increase  $d$  gradually from the critical value  $d_1^c$ , and the spatially averaged susceptible population is plotted against time in Fig. 13a. It is observed that the spatially averaged susceptible population reaches a stationary value after the initial transient oscillations. However, the duration of transient time decreases with an increase in the value of dispersal rate  $d$ . Moreover, this transient time duration to arrive at the stationary state increases exponentially as  $d$  tends to  $d_1^c$  from above. The transient duration as  $d$  tends to  $d_1^c$  can be described by a power law as shown in Fig. 13b.

The point representing  $\beta = 48.5$  and  $d = 2.88$  lies in the Turing domain of system (10), and the corresponding transient pattern is shown in Fig. 14a. Also, the phase diagram of the spatially averaged populations is shown in Fig. 14b. It is observed that both the populations spend a considerable time oscillating initially and then settle at a point (magenta-colored asterisk) away from the center of the oscillation. Next we choose a representative point  $\beta = 48.5$  and  $d = 2.5$  from the stable domain of the local system (10) close to the temporal Hopf threshold. For these choice of parameters, system (10) possesses a homogeneous stationary solution corresponding to the endemic equilibrium  $P_1^*$ . However, the evolution of the solution oscillates around the homogeneous endemic steady state for a long time. The solution characteristics during the transient state shown in Fig. 15 confirm that both the

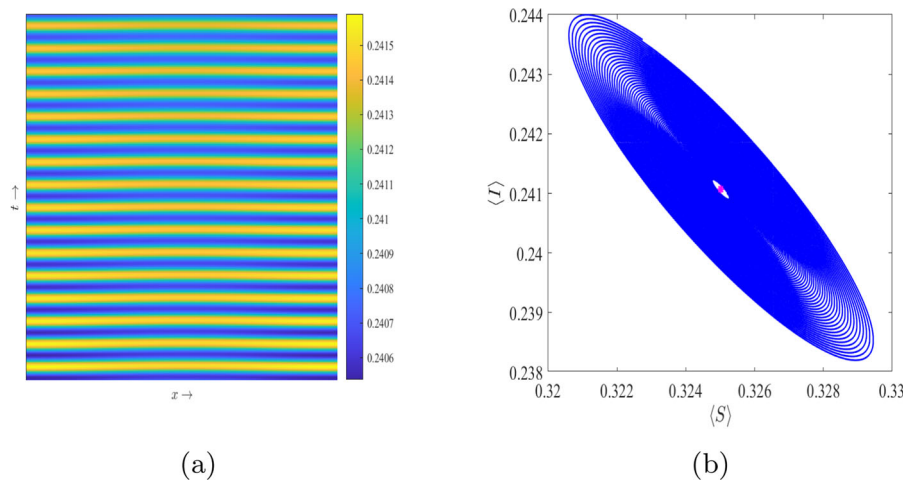
**Fig. 14** Transient characteristics of the local system (10) for  $\beta = 48.5$  and  $d = 2.88$ : **a** space–time transient pattern of the infected population, **b** phase diagram of the spatially averaged populations. Other parameter values are given in the caption of Fig. 13. The left panel shows various non-resonant infectious peaks over the spatial domain in the transient state



(a)

(b)

**Fig. 15** Transient characteristics of system (10) for  $\beta = 48.5$  and  $d = 2.5$ : **a** space–time transient pattern of the infected population, **b** phase diagram of the spatially averaged populations up to 1200 time unit. Other parameter values are given in the caption of Fig. 13. The left panel depicts multiple epidemic peaks in the transient state of the local system (10)



(a)

(b)

populations oscillate for a considerable time around the homogeneous steady state (shown by the magenta-colored asterisk in Fig. 15b).

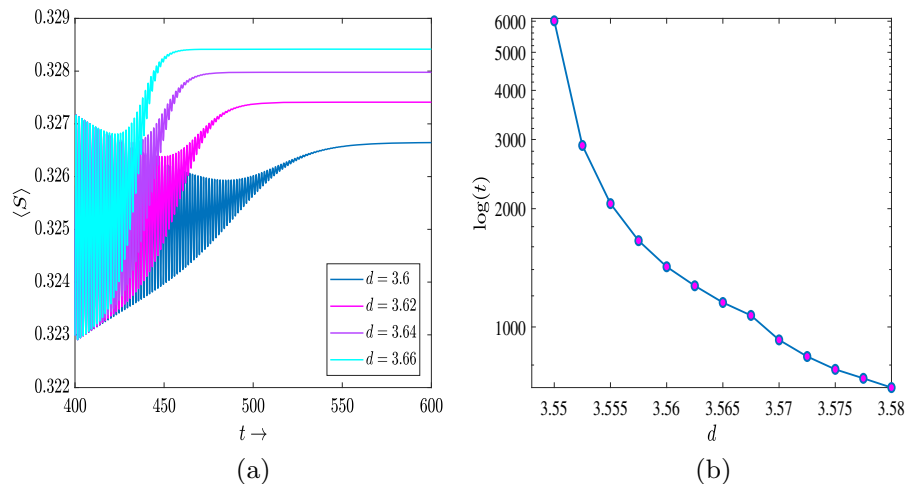
Finally, we analyze the nonlocal system (20) for the transient dynamics using the same initial condition (31). The Turing threshold for  $\beta = 48.5$  and  $\delta = 0.6$  is  $d_1^T \approx 3.531$ . Using similar approach as that of the local model, we examine the dependency of the transient duration on the spatial dispersal rate  $d$ . In this case, we observed similar transient characteristics as that of the local model (see Fig. 14). It is observed that as  $d$  decreases gradually toward  $d_1^T$ , system (20) oscillates for a relatively longer duration of time before settling to the stationary spatially heterogeneous solution. The spatial average of the susceptible population against time is plotted for four different values of  $d$  in Fig. 16a. It is evident that a higher value of  $d$  results in faster convergence to the stationary state of system (20). Further,

the nonlocal system exhibits long transient characteristics similar to its local counterpart as  $d$  tends to  $d_1^T$  from above. The corresponding power law of the transient duration is presented in Fig. 16b.

## 7 Discussion and conclusions

In the current body of literature, the spatio-temporal dynamics of infectious diseases have been examined considering only the local transmission of the causative agents. The process of disease transmission, however, is not confined to the host's geographic location, and frequently, distant susceptible are at risk of contracting the illness. There are very few studies that model this issue of nonlocal disease spread. As a result, the spatio-temporal dynamics of the disease transmission taking into account the possibility of nonlocal transmission is

**Fig. 16** Transient dynamics of the nonlocal model (20) for  $\beta = 48.5$  and  $\delta = 0.6$ : **a** temporal evolution of the spatially averaged susceptible population for different dispersal rate and **b** plot of transient time duration in the logarithmic scale against  $d$ . Other parameter values are  $\Lambda = 1$ ,  $\mu = 1$ ,  $\sigma = 1.8$ ,  $\gamma = 1$ , and  $d_2 = 1$



still not elucidated to date. Along with the nonlocality of disease transmission, nonlinearity in per-capita disease incidence rate as well as understanding of spatial distribution of susceptible and infected individuals are other significant but less explored topics in mathematical epidemiology. This study primarily focuses on the asymptotic analysis of a nonlocal reaction–diffusion SIS-type epidemic model with a nonlinear incidence rate. In particular, we analyzed various spatio-temporal patterns exhibited by the proposed model.

First, we analyzed the asymptotic profile of the temporal SIS model with nonlinear per-capita disease incidence. Interestingly, the model shows two local bifurcations, namely saddle-node and subcritical Hopf bifurcations. It also shows global homoclinic bifurcation with disease transmission rate  $\beta$  as the bifurcating parameter. Therefore, unlike SIS models with linear per-capita incidence rate, the model under consideration exhibits periodic solutions which eventually disappear at the homoclinic loop bifurcation. Moreover, the system exhibits a bistable nature after  $\beta$  crosses the threshold of homoclinic bifurcation. Second, we extend the model to take into account the random movement of the individuals by introducing a one-dimensional Laplacian diffusion term. We restricted ourselves to one-dimensional space for simplicity of mathematical calculations involved with the model in the presence of nonlocal disease transmission. The Turing instability condition of the homogeneous steady state  $P_1^*$  is derived through linear stability analysis. Based on both mathematical analysis and numerical simulation, our findings show that along with homogeneous steady

states, the spatio-temporal model (10) admits both stationary patchy distribution and various dynamic distribution of both susceptible and infected populations. The exhibited dynamic distribution of the population by system (10) depends upon the choice of parametric domain (see Fig. 4) and is characterized as the chaotic, quasi-periodic, or periodic. Epidemiologically, the formation of the Turing pattern (Fig. 5) explains the formation of multiple stationary patches observed in realistic scenarios to minimize the risk of infection through a moderate dispersal rate. On the other hand, formation of the chaotic patterns due to irregular oscillations of the population densities with respect to both space and time can be observed when the population continuously migrates in neighboring patches with a lower dispersal rate. The exhibited dynamic patterns by system (10) are sensitive to its initial condition, but the qualitative structure of the patterns is preserved for a particular parametric set.

Finally, we extend the model to incorporate the possibility of the nonlocal transmission of the diseases using a spatial kernel function. The nonlocal model is also investigated for the Turing instability criterion and numerical simulations are conducted to examine the influence of nonlocal transmission. It has been observed that the Turing curve shifts upward as we increase the extent of nonlocal disease transmission  $\delta$ . As a result, the Hopf and stable domains of the  $\beta$ - $d$  plain (sketched in Fig. 9) expands gradually with an increment in  $\delta$ . The epidemiological implementation of the result is that when the disease can spread in a wider spatial range, individual requires a higher dispersal rate to

form multiple stationary patches. This finding has also been validated by the change in the number of stationary patches, exhibited by system (20) in a fixed spatial domain due to an increment in  $\delta$ , plotted in Fig. 12. It is observed that the number of stationary patches decreases due to an increment in the nonlocal infection extent. Further, qualitative changes in the spatial distribution of susceptible and infected for different values of  $\delta$ , leading to several dynamic spatio-temporal patterns have been observed for the nonlocal system (20). Comparing Figs. 4 and 9b, one may observe that system (20) possesses a larger parametric domain of the homogeneous disease-free steady state. Moreover, the parametric domain of the homogeneous disease-free steady state increases with the nonlocal extent parameter  $\delta$  and it may be observed even in the Turing–Hopf domain. Clearly, nonlocality in the disease transmission stabilizes the oscillatory spatial distribution in the Hopf domain. In addition to this, the stable domain of the nonlocal system (20), where the system possesses a homogenous endemic steady state, also expands proportionally with  $\delta$ . Finally, a smaller portion in the Hopf domain of the nonlocal system (20) still possesses oscillatory solutions (see Fig. 9b). Epidemiologically, one may conclude that the nonlocal range of disease transmission can break the stationary patchy distribution of the population and transform them into either oscillatory or spatially homogeneous steady states. Therefore, the nonlocal infection can induce chaotic behavior or break the heterogeneous spatial distribution into homogeneous steady states.

In addition to the spatio-temporal dynamics, our study also explores the idea of “long transient” behavior observed in many systems [42]. The dynamics of an epidemic model away from its attractors are particularly helpful in combating the emergence or re-emergence of many pathogens or parasites [43]. It is also helpful in characterizing the initial pattern of the spread of the disease, forecasting infected cases and death tolls, etc. In this study, we have demonstrated transient dynamics through numerical simulation. It is observed that the local system (10) exhibits long transient dynamics as  $d$  tends to  $d_1^c$  from above and the associated power law of the transient duration is plotted in Fig. 13b. Moreover, for  $d$  below  $d_1^c$ , the local system (10) exhibits a time-periodic spatial distribution of the susceptible and infected for a long duration (as shown in Fig. 15). The duration of the transient state depends on the initial densities of susceptible and infected. Further-

more, it has been observed that the transient duration becomes relatively brief for points sufficiently away from the temporal Hopf threshold in the  $\beta$ - $d$  parametric plane (referred in Fig. 9b). A similar kind of transient dynamics is also observed for the corresponding nonlocal infection model (20). Epidemiologically, this time-periodic nature of the spatial pattern as presented in Fig. 15 signifies multiple epidemic peaks appearing in emerging infectious diseases. Of course, the number of time-periodic waves depends on the initial distribution of the infected and susceptible populations. On the contrary, the epidemic may also emerge as “non-resonant peaks” in which epidemic waves apparently occur at an arbitrary frequency and amplitude [46]. Figure 14a depicts this pattern in a spatio-temporal scale at its transient stage. Moreover, Figs. 13 and 16 explain the source of long transient dynamics for both the local and nonlocal systems, respectively. It is also observed that the individual dispersal rate determines the nature of the initial transient dynamics of the epidemic.

Interestingly, the density of the infected population may be out of control due to the spatio-temporal chaos exhibited by both the local and nonlocal systems. Existence of spatio-temporal chaos can be interpreted as the localized outbreak of the disease from one location to another induced by the long-distance transmission of the disease. For a given set of other parameter values, the spatio-temporal chaotic behavior is observed when the rates of mobility of the susceptible and infected are close to each other. Moreover, the top-hat-type transmission kernel used in this study increases the Hopf domain gradually with an increment in  $\delta$ . But in the real world, the density of the infected population must be under control for a sustainable health system. Also, estimating the kernel type from the empirical data is very difficult, but it is an important problem. Therefore, it would be interesting to investigate the spatial dynamics with some other types of spatial kernels, namely Gaussian ( $\Psi_\delta \propto \exp(-A\delta^2)$ ), exponential ( $\Psi_\delta \propto \exp(-A\delta)$ ), power law ( $\Psi_\delta \propto \delta^{-A}$ ), etc. [5]. Moreover, the nonlocal model (20) with top-hat kernel does not produce spatial Hopf phenomenon. Thus, it would be interesting to investigate the same with other kinds of Kernels or disease incidence rates. Finally, this model can be further extended by introducing a predator community that consumes an infected or parasite-induced species. Accordingly, it would be another compelling research prospect to study the spatio-temporal patterns exhibited in a parasite-induced prey–predator

ecosystem. We shall consider these open problems systematically in our future studies.

**Acknowledgements** The author Dhiraj Kumar Das gratefully acknowledges the financial support provided by the Science and Engineering Research Board, Government of India, through the National Postdoctoral Fellowship scheme under the file number PDF/2021/001915, dated January 4, 2022.

**Data availability** Data sharing is not applicable to this article as no datasets were generated or analyzed during the current study. However, the codes or algorithms used in the simulation will be made available on specific requests.

## Declaration

**Conflict of interest** The authors state here that they have no known competing financial interests or personal relationships that could have appeared to influence the work accounted for in this paper.

## References

1. Kermack, W.O., McKendrick, A.G.: A contribution to the mathematical theory of epidemics. Proc. Roy. Soc. Lond. Ser. A Contain. Pap. Math. Phys. Charact. **115**(772), 700–721 (1927)
2. Ghosh, S., Volpert, V., Banerjee, M.: An epidemic model with time-distributed recovery and death rates. Bull. Math. Biol. **84**(8), 78 (2022)
3. Das, D.K., Kar, T.: Global dynamics of a tuberculosis model with sensitivity of the smear microscopy. Chaos Solitons Fractals **146**, 110879 (2021)
4. d’Onofrio, A.: A note on the global behaviour of the network-based sis epidemic model. Nonlinear Anal. Real World Appl. **9**(4), 1567–1572 (2008)
5. Keeling, M.J., Rohani, P.: Modeling Infectious Diseases in Humans and Animals. Princeton University Press (2008)
6. Wang, Z., Bauch, C.T., Bhattacharyya, S., d’Onofrio, A., Manfredi, P., Perc, M., Perra, N., Salathé, M., Zhao, D.: Statistical physics of vaccination. Phys. Rep. **664**, 1–113 (2016)
7. Li, H.-J., Xu, W., Song, S., Wang, W.-X., Perc, M.: The dynamics of epidemic spreading on signed networks. Chaos Solitons Fractals **151**, 111294 (2021)
8. d’Onofrio, A., Manfredi, P.: Behavioral sir models with incidence-based social-distancing. Chaos Solitons Fractals **159**, 112072 (2022)
9. Jana, S., Nandi, S.K., Kar, T.: Complex dynamics of an sir epidemic model with saturated incidence rate and treatment. Acta Biotheor. **64**(1), 65–84 (2016)
10. Van den Driessche, P., Watmough, J.: Reproduction numbers and sub-threshold endemic equilibria for compartmental models of disease transmission. Math. Biosci. **180**(1–2), 29–48 (2002)
11. Ruan, S., Wang, W.: Dynamical behavior of an epidemic model with a nonlinear incidence rate. J. Differ. Equ. **188**(1), 135–163 (2003)
12. Banerjee, M., Volpert, V.: Spatio-temporal pattern formation in Rosenzweig–Macarthur model: effect of nonlocal interactions. Ecol. Complex. **30**, 2–10 (2017)
13. Malchow, H., Hilker, F.M., Siekmann, I., Petrovskii, S.V., Medvinsky, A.B.: Mathematical models of pattern formation in planktonic predation–diffusion systems: a review. Aspects Math. Modell. **8**, 1–26 (2008)
14. Dey, S., Banerjee, M., Ghorai, S.: Analytical detection of stationary turing pattern in a predator–prey system with generalist predator. Math. Modell. Nat. Phenom. **17**, 33 (2022)
15. Paquin-Lefebvre, F., Nagata, W., Ward, M.J.: Pattern formation and oscillatory dynamics in a two-dimensional coupled bulk-surface reaction–diffusion system. SIAM J. Appl. Dyn. Syst. **18**(3), 1334–1390 (2019)
16. Zhang, L., Liu, J., Banerjee, M.: Hopf and steady state bifurcation analysis in a ratio-dependent predator–prey model. Commun. Nonlinear Sci. Numer. Simul. **44**, 52–73 (2017)
17. Murray, J.D.: Mathematical Biology II: Spatial Models and Biomedical Applications, vol. 3. Springer (2001)
18. Raffel, T.R., Martin, L.B., Rohr, J.R.: Parasites as predators: unifying natural enemy ecology. Trends Ecol. Evol. **23**(11), 610–618 (2008)
19. Malchow, H., Petrovskii, S., Venturino, E.: Spatiotemporal Patterns in Ecology and Epidemiology: Theory, Models, and Simulation. Chapman and Hall/CRC (2008)
20. González, E., Villena, M.J.: On the spatial dynamics of vaccination: a spatial sirs-v model. Comput. Math. Appl. **80**(5), 733–743 (2020)
21. Allen, L.J., Bolker, B.M., Lou, Y., Nevai, A.L.: Asymptotic profiles of the steady states for an sis epidemic reaction–diffusion model. Discrete Contin. Dyn. Syst. **21**(1), 1 (2008)
22. Sun, G.-Q., Jusup, M., Jin, Z., Wang, Y., Wang, Z.: Pattern transitions in spatial epidemics: mechanisms and emergent properties. Phys. Life Rev. **19**, 43–73 (2016)
23. Li, L.: Patch invasion in a spatial epidemic model. Appl. Math. Comput. **258**, 342–349 (2015)
24. Zhang, G.-B., Li, Y., Feng, Z.: Exponential stability of traveling waves in a nonlocal dispersal epidemic model with delay. J. Comput. Appl. Math. **344**, 47–72 (2018)
25. Tian, B., Yuan, R.: Traveling waves for a diffusive seir epidemic model with non-local reaction. Appl. Math. Model. **50**, 432–449 (2017)
26. Maidana, N.A., Yang, H.M.: Spatial spreading of West Nile Virus described by traveling waves. J. Theor. Biol. **258**(3), 403–417 (2009)
27. Adimy, M., Chekroun, A., Kazmierczak, B.: Traveling waves for reaction–diffusion PDE coupled to difference equation with nonlocal dispersal term and time delay. Math. Model. Nat. Phenom. **17**, 17 (2022)
28. Liu, Z., Shen, Z., Wang, H., Jin, Z.: Analysis of a local diffusive sir model with seasonality and nonlocal incidence of infection. SIAM J. Appl. Math. **79**(6), 2218–2241 (2019)
29. Liu, W.-M., Levin, S.A., Iwasa, Y.: Influence of nonlinear incidence rates upon the behavior of sirs epidemiological models. J. Math. Biol. **23**(2), 187–204 (1986)
30. Liu, W.-M., Hethcote, H.W., Levin, S.A.: Dynamical behavior of epidemiological models with nonlinear incidence rates. J. Math. Biol. **25**(4), 359–380 (1987)
31. Pal, S., Ghorai, S., Banerjee, M.: Analysis of a prey–predator model with non-local interaction in the prey population. Bull. Math. Biol. **80**(4), 906–925 (2018)

32. Pal, S., Ghorai, S., Banerjee, M.: Effect of kernels on spatio-temporal patterns of a non-local prey-predator model. *Math. Biosci.* **310**, 96–107 (2019)
33. Manna, K., Volpert, V., Banerjee, M.: Pattern formation in a three-species cyclic competition model. *Bull. Math. Biol.* **83**(5), 1–35 (2021)
34. Banerjee, M., Volpert, V.: Prey-predator model with a non-local consumption of prey. *Chaos Interdiscip. J. Nonlinear Sci.* **26**(8), 083120 (2016)
35. Manna, K., Volpert, V., Banerjee, M.: Dynamics of a diffusive two-prey-one-predator model with nonlocal intra-specific competition for both the prey species. *Mathematics* **8**(1), 101 (2020)
36. Manna, K., Banerjee, M.: Spatiotemporal pattern formation in a prey-predator model with generalist predator. *Math. Modell. Nat. Phenom.* **17**, 6 (2022)
37. Autry, E.A., Bayliss, A., Volpert, V.A.: Biological control with nonlocal interactions. *Math. Biosci.* **301**, 129–146 (2018)
38. Wang, T.: Dynamics of an epidemic model with spatial diffusion. *Physica A* **409**, 119–129 (2014)
39. Sun, G.-Q., Jin, Z., Liu, Q.-X., Li, L.: Chaos induced by breakup of waves in a spatial epidemic model with nonlinear incidence rate. *J. Stat. Mech. Theory Exp.* **2008**(08), 08011 (2008)
40. Hastings, A., Higgins, K.: Persistence of transients in spatially structured ecological models. *Science* **263**(5150), 1133–1136 (1994)
41. Hastings, A., Abbott, K.C., Cuddington, K., Francis, T., Gellner, G., Lai, Y.-C., Morozov, A., Petrovskii, S., Scranton, K., Zeeman, M.L.: Transient phenomena in ecology. *Science* **361**(6406), 6412 (2018)
42. Morozov, A., Abbott, K., Cuddington, K., Francis, T., Gellner, G., Hastings, A., Lai, Y.-C., Petrovskii, S., Scranton, K., Zeeman, M.L.: Long transients in ecology: theory and applications. *Phys. Life Rev.* **32**, 1–40 (2020)
43. Tao, Y., Hite, J.L., Lafferty, K.D., Earn, D.J., Bharti, N.: Transient disease dynamics across ecological scales. *Thyroid Res.* **14**(4), 625–640 (2021)
44. Hethcote, H.W., van den Driessche, P.: Some epidemiological models with nonlinear incidence. *J. Math. Biol.* **29**(3), 271–287 (1991)
45. Moghadas, S.M., Gumel, A.B.: Global stability of a two-stage epidemic model with generalized non-linear incidence. *Math. Comput. Simul.* **60**(1–2), 107–118 (2002)
46. Bauch, C.T., Earn, D.J.: Transients and attractors in epidemics. *Proc. Roy. Soc. Lond. Ser B Biol. Sci.* **270**(1524), 1573–1578 (2003)

**Publisher's Note** Springer Nature remains neutral with regard to jurisdictional claims in published maps and institutional affiliations.

Springer Nature or its licensor (e.g. a society or other partner) holds exclusive rights to this article under a publishing agreement with the author(s) or other rightsholder(s); author self-archiving of the accepted manuscript version of this article is solely governed by the terms of such publishing agreement and applicable law.